

**Shining Light on Dark Matter,
One Photon at a Time**

by

Brandon Leigh Allen

Submitted to the Department of Physics
in partial fulfillment of the requirements for the degree of

Doctorate of Science in Physics

at the

MASSACHUSETTS INSTITUTE OF TECHNOLOGY

June 2019

© Massachusetts Institute of Technology 2019. All rights reserved.

Author
Department of Physics
May 18, 2019

Certified by
Christoph E.M. Paus
Professor
Thesis Supervisor

Accepted by
Nergis Mavalvala
Associate Department Head for Education

**Shining Light on Dark Matter,
One Photon at a Time**

by

Brandon Leigh Allen

Submitted to the Department of Physics
on May 18, 2019, in partial fulfillment of the
requirements for the degree of
Doctorate of Science in Physics

Abstract

A search is conducted for new physics in final states containing a photon and missing transverse momentum in proton-proton collisions at $\sqrt{s} = 13$ TeV. The data collected by the CMS experiment at the CERN LHC correspond to an integrated luminosity of 35.9 inverse femtobarns. No deviations from the predictions of the standard model are observed. The results are interpreted in the context of dark matter production and limits on new physics parameters are calculated at 95% confidence level. For the two simplified dark matter production models considered, the observed (expected) lower limits on the mediator masses are both 950 (1150) GeV for 1 GeV dark matter mass.

Thesis Supervisor: Christoph E.M. Paus

Title: Professor

Acknowledgments

This is the acknowledgements section. You should replace this with your own acknowledgements.

Contents

1 Global Event Reconstruction	9
1.1 Particle Flow Elements	11
1.1.1 Tracks	11
1.1.2 Primary Vertexing	12
1.1.3 Secondary Vertexing	13
1.1.4 ECAL Superclusters	13
1.1.5 HCAL Clusters	14
1.1.6 Muon Segments	15
1.1.7 Isolation	15
1.2 Particle Identification	17
1.2.1 Muons	17
1.2.2 Electrons	18
1.2.3 Isolated Photons	19
1.2.4 Hadrons	21
1.2.5 Jets	23
1.2.6 Missing Transverse Energy	24
1.3 Reconstruction Issues	25
1.3.1 ECAL gain-switch effect	25
1.3.2 ECAL Barrel Spikes Phenomenology	27
2 The Monophoton Analysis	33
2.1 Dataset	34
2.1.1 Trigger Efficiency	35

2.1.2	Pileup Reweighting	36
2.2	Event Selection	38
2.2.1	Signal Regions	39
2.2.2	Control Regions	39
2.2.3	Proxy Samples	40
2.2.4	Measurement Samples	41
2.3	Photon ID Efficiency Scalefactor	41
2.3.1	e/γ ID Efficiency	42
2.3.2	γ -specific ID Efficiency	47
2.4	Misidentified electrons	52
2.5	Misidentified hadrons	55
2.6	Irreducible backgrounds	57
2.6.1	Simulation of $V+\gamma$ Processes	57
2.6.2	Data-driven Control Regions	64
2.7	Beam halo	69
2.8	Spikes	74
2.9	Minor SM Backgrounds	76
2.10	Statistical Interpretation	76
2.11	Results	77
2.11.1	Pre-fit and post-fit distributions	77
2.11.2	Limits	81

Chapter 1

Global Event Reconstruction

In the previous chapter, we discussed the interactions of particles with the individual subdetectors and how these generate electrical signals. Now, we shall discuss the reverse process, namely reconstructing the individual particles or physics objects from the electrical signals recorded by the subdetectors.

Traditionally, each class of physics object is reconstructed using information from a single subdetector: muons from the muon chambers, isolated photons and electrons from the ECAL, jets and missing transverse energy from the HCAL, and secondary vertices from τ lepton and b hadron decays from the tracker. However, as depicted in Figure 1-1, each type of particle interacts with multiple different subdetectors and this information is lost unless the information from all the subdetectors is combined into a single global event description.

The particle flow (PF) algorithm leverages the fine angular granularity of the calorimeters and the excellent momentum resolution of the inner tracker and muon chambers to greatly improve the reconstruction of physics objects and include soft particles that would otherwise be ignored. This is especially advantageous for jet energy measurements as roughly 62% of the jet energy is carried by charged hadrons, approximately 27% by photons, around 10% by neutral hadrons, and about 1.5% by neutrinos.

The distinguishing feature of the PF algorithm is to combine multiple detector signals together into a single PF candidate. The input detector signals are the tracks,

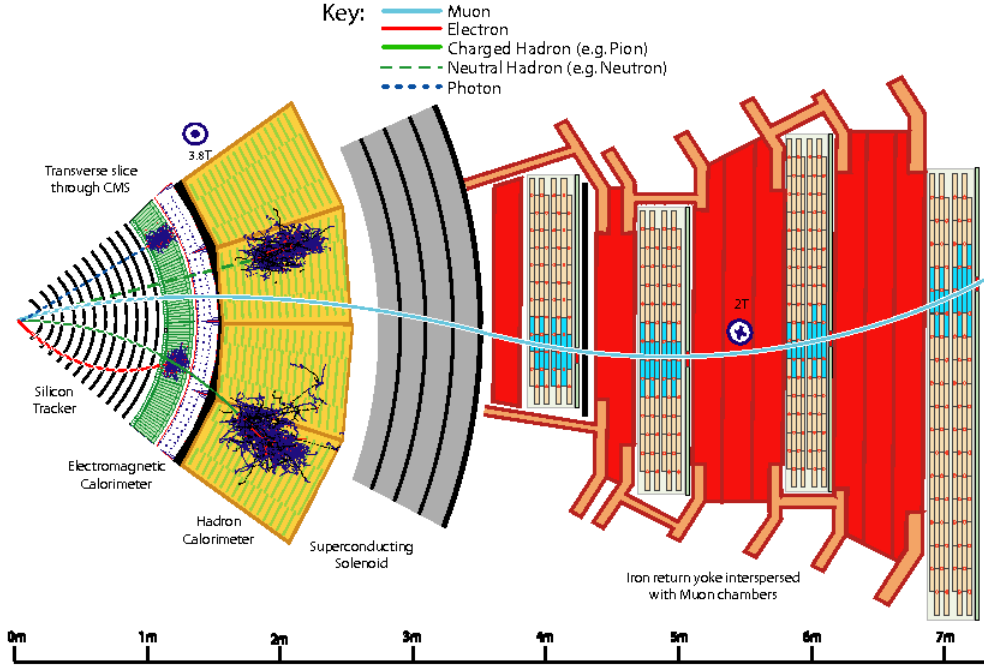


Figure 1-1: A sketch of a transverse slice of the CMS detector showing particle interactions from the interaction point to the muon detector. Reprinted from Reference [1].

vertices, calorimeter clusters, and muon segments described in Section 1.1. Based on their proximity in the $\eta\text{-}\phi$, these PF elements are combined into muons, electrons, photons, and hadrons. Muon segments are combined with inner tracks to produce muons, inner tracks are combined with calorimeter clusters to produce electrons and charged hadrons, and calorimeter clusters are correlated to produce photons and neutral hadrons.

The PF algorithm reconstructs particles in regions of the detectors called blocks following the steps described in Section 1.2. After each step any PF elements associated to a PF candidate are removed from the block. For example, clusters associated with photons will not be used when reconstructing neutral hadrons. After all PF candidates are identified, they can be combined into event-wide variables such as jets and the missing transverse energy as described in Sections 1.2.5 and 1.2.6, respectively.

1.1 Particle Flow Elements

1.1.1 Tracks

The Combinatorial Track Finder software is used to reconstruct tracks in an iterative inside-out process. Initial iterations search for tracks that are easy to find, e.g. those with high p_T , and hits associated with these tracks are removed for later iterations, reducing the combinatorial complexity and simplifying the search for more difficult tracks, e.g. greatly displaced ones.

The first step is to form seeds based on pixel hits, double strip hits containing 3D information, and an estimate of the beam spot. Earlier iterations require three pixel hits while later iterations gradually loosen the requirements. The final iterations specifically target increased muon tracking efficiency by including information from the muon chambers.

Next, a Kalman filter is used to find additional hits consistant with the evolution of the track seeds through the rest of the tracker, accounting for the magnetic field, energy loss due to ionization, and multiple scattering. The five parameters used for the helical trajectory evolution are the curvature ρ , the azimuthal angle ϕ_0 , the transverse impact parameter d_0 , the longitudinal impact parameter z_0 , and $\lambda = \cot \theta$, where θ is the polar angle.

After propagating the track through all layers of the detector and finding all associated hits, a Kalman fitter and smoother is used to refit the overall trajectory while a fourth-order Runge-Kutta method is used to extrapolate the trajectory between successive hits. To reduce the fraction of fake tracks, various quality requirements concerning the number of missing hits, the reduced χ^2 of the fit, and compatibility with a primary vertex are applied before proceeding to the next iteration.

Track reconstruction for electrons is more complicated as the Kalman filter is not a good description because of the high rate of non-Gaussian energy loss due to brehmsstrahlung these tracks experience within the tracker. To improve the electron reconstruction efficiency, the electron seed collection is filled both by looking outside-in for ECAL superclusters (see Section 1.1.4) consistant with track seeds and inside-

out track seeds consistent with superclusters. A Gaussian Sum Filter (GSF) defined to approximate the Bethe-Heitler energy-loss distribution is used to fit the trajectory of electron tracks.

1.1.2 Primary Vertexing

A deterministic annealing (DA) algorithm is used to associate tracks to primary vertices. Tracks must pass additional requirements on the transverse impact parameter d_0 , the number of strip and pixel hits, and the reduced χ of the trajectory fit to be considered when finding primary vertices. The most probable vertex positions at an artificial temperature T are determined by the minimization of the “free energy”

$$F = -T \sum_i^{N_T} \ln \sum_j^{N_V} p_{ij} \rho_j \exp \left[-\frac{1}{T} \left(\frac{z_i^T - z_j^V}{\sigma_i^z} \right)^2 \right] \quad (1.1)$$

where the z_j^V are the vertex positions with weights ρ_j , the z_i^T and σ_i^z are the longitudinal impact parameters and the corresponding uncertainties of the tracks, and the p_{ij} are the probabilities of assigning the track i of N_T to the vertex j of N_V .

The DA algorithm starts with a single vertex at a very high temperature that is gradually decreased. The free energy F is minimized with respects to z_j^K at each new temperature and a vertex is split in two whenever T falls below its critical temperature

$$T_C^j = 2 \sum_i \frac{p_i p_{ij}}{(\sigma_i^z)^2} \left(\frac{z_i^T - z_j^V}{\sigma_i^z} \right)^2 \Bigg/ \sum_i \frac{p_i p_{ij}}{(\sigma_i^z)^2}. \quad (1.2)$$

The annealing procedure with vertex splitting continues down to $T = 4$ and the final assignment of tracks to vertices is performed at $T = 1$ without any further splitting. The vertex designated as *the* primary vertex (PV) of the hard scattering is the one which maximizes

$$S_T = \sum_i (p_T^i)^2 + (p_T^{\text{miss}})^2, \quad (1.3)$$

where p_T^i is the transverse momentum of a track assigned to the vertex and p_T^{miss} is the magnitude of the momentum imbalance in the transverse plane for the vertex.

1.1.3 Secondary Vertexing

Long-lived particles such as b hadrons and τ leptons often produce charged particles in their decays. These charged particles are traced to a secondary vertex at the location of the decay, which is identified by the inclusive vertex fitter (IVF) algorithm.

The IVF procedure begins by selecting seed tracks with a 2D impact parameter significance $\sigma_{d_0} \geq 1.2$ and a 3D impact parameter $\sqrt{d_0^2 + z_0^2} \geq 50 \mu\text{m}$. Tracks are assigned to a secondary vertex based on their opening angle with the seed track and distance at closest approach, with the additional stipulation that this distance be smaller for the secondary vertex than for the primary vertex.

To determine the precise position of the secondary vertices, the associated tracks are fitted with the adaptive vertex fitter and any vertices with a flight distance significance less than a certain threshold are discarded. At this point, a track is unassociated from a secondary vertex if the angular distance between the track and the secondary vertex flight direction is greater than 0.4 and if the track's distance at closest approach is larger than the magnitude of its impact parameter.

The secondary vertex position is refitted after track cleaning if there are still at least two tracks associated with the vertex. The last stage of cleaning removes a secondary vertex if it shares at least 20% of its tracks with another and the flight distance significance between the two is less than ten.

1.1.4 ECAL Superclusters

Due to the large amount of material in the tracker, electrons often emit bremsstrahlung photons, photons often convert to electron-positron pairs, and the brehmsstrahlung photons and converted electrons often undergo further conversion and brehmsstrahlung before reaching the ECAL. Because of the bending of electron trajectories in the magnetic field, the resulting electromagnetic (EM) shower is significantly spread in the ϕ -direction and collimated in the η -direction. The ECAL reconstruction algorithm combines the basic cluster from each showered particle into a supercluster representing the initial electron or photon from the hard scattering.

The first step is the identification of a seed crystal with greater transverse energy than its immediate neighbors and above a predefined minimum threshold. The energy of each crystal is determined from calibration constants combined with the amplitude and peak time obtained by fitting the pulse shape of the ten time samples surrounding the triggering bunch crossing.

In the barrel, a supercluster starts with a 5×1 array of crystals in the $\eta\text{-}\phi$ plane centred on the seed crystal. The array is extended around the seed crystal in the ϕ -direction up to $|\Delta\phi| \leq 0.3$ if the energy of the additional crystals exceeds a certain threshold. The contiguous array is grouped into distinct basic clusters each containing a seed array with energy greater than another threshold. The supercluster is the collection of basic threshold found in the $\eta\text{-}\phi$ region centered on the initial seed crystal. Since the crystals in the endcaps are arranged in an $x\text{-}y$ grid, clustering here uses fixed 5×5 matrices of crystals. After a seed cluster is identified, additional, partially overlapping 5×5 matrices are added if their centroid lies within $|\Delta\eta| \leq 0.07$ and $|\Delta\phi| \leq 0.3$. For unconverted photons, both methods produce superclusters that are simple 5×5 matrices.

1.1.5 HCAL Clusters

The purpose of clustering in the HCAL is to measure the energy and direction of neutral hadrons, disentangle neutral hadrons from charged hadron energy deposits, and improve the energy measurement for charged hadrons with poorly reconstructed tracks. Similar to the supercluster algorithm, a cluster in the HCAL is first identified by a seed cell with greater transverse energy than its immediate neighbors and above a predefined minimum threshold. This seed is then grown into a topological cluster by adding cells with at least a corner in common with a cell already in the cluster and energy above twice the noise threshold.

An iterative Gaussian mixture model is used to break each topological cluster of M individual cells is broken into N energy deposits corresponding to individual particles, where N is the number of seeds. Each energy deposit is modeled as a Gaussian distribution \mathcal{N} with amplitude A_i , mean $\vec{\mu}_i$ in the $\eta\text{-}\phi$ plane, and width

σ fixed by the calorimeter resolution. The expected fraction f_{ji} of the energy E_j measured in the cell at position \vec{c}_j from the i th energy deposit is

$$f_{ji} = \frac{\mathcal{N}(\vec{c}_j|A_i, \vec{\mu}_i, \sigma)}{\sum_k^N \mathcal{N}(\vec{c}_j|A_k, \vec{\mu}_k, \sigma)}. \quad (1.4)$$

The amplitude and position of each energy deposit are determined by an analytical maximum-likelihood fit to be

$$A_i = \sum_j^M f_{ji} E_j \quad \left| \quad \vec{\mu}_i = \sum_j^M f_{ji} E_j \vec{c}_j \right. \quad (1.5)$$

where the initial values are the energy and position of the seeds. The process of calculating energy fractions f_{ji} and fitting for the amplitudes A_i and positions $\vec{\mu}_i$ is repeated until convergence, at which point they are taken as the cluster parameters.

1.1.6 Muon Segments

Muon segments are reconstructed from the hits in the muon chambers using a Kalman filter in a similar manner to that described for the inner tracker in Section 1.1.1. A full track constructed in this way is referred to as a standalone muon.

1.1.7 Isolation

While not a physics object persay, isolation is a key concept of the PF algorithm that distinguishes prompt leptons and photons originating in the hard scattering from those originating in the decays of hardrons during the parton shower. The latter are surrounded by a large amount of additional hadrons while the former have little hadronic activity in their vicinity, originating mainly from the pileup vertices.

The isolation of a prompt object is the total amount of energy due to additional particles within an annulus of radius $0.01 < \Delta R < 0.4$ around the prompt object, where the lower bound avoids including the prompt object and its radiation in the sum. The isolation is calculated using either the raw energy deposits in the subdetectors or the four-momenta of the PF candidates surrounding the prompt object

depending the stage of the PF algorithm. Prompt objects are required to have an isolation value below a certain threshold, rejecting hadrons misidentified as leptons and photons as well as non-prompt leptons and photons.

The isolation calculation is usually split into three different components based on the types of particles that contribute energy. The photon isolation I_γ is the E_T sum of the PF photons defined in Section 1.2.3 while the charged hadron and neutral hadron isolations I_{CH} and I_{NH} are the p_T sums of the PF charged and neutral hadrons defined in Section 1.2.4, with the additional stipulation that charged hadrons be associated with the primary vertex.

In events with very few tracks, such as one with a single high p_T photon and a large momentum imbalance, it is possible that the identified primary vertex does not correspond to the pp interaction from which the photon object originates because the photon does not figure into the primary vertex calculation from Section 1.1.2. In such cases, the photon object can be surrounded by charged hadrons and still appear isolated under the standard charged hadron isolation. A conservative measure to address such misidentification is to replace I_{CH} with the maximum of the PF charged hadron isolations computed over all reconstructed vertices, e.g. the maximum charged hadron isolation $I_{\text{CH}}^{\max} = \max_{\text{vertices}} I_{\text{CH}}$.

To reduce the pileup dependence of these variables, the median energy density ρ of the pileup interactions in the isolation cone is calculated using the effective areas given in Table 1.1 and subtracted from each isolation sum. Additionally, since the rate of the charged particles originating from pileup interactions is about twice as large as the corresponding rate of the neutral particles, the pileup isolation I_{PU} is defined as the half the p_T sum of the PF charged hadrons *not* associated with the primary vertex. Often selections are placed on the individual isolation components when selecting prompt photons, while the relative combined PF isolation

$$I_{\text{PF}}^{\text{rel.}} = \left(I_{\text{CH}} + \max \left\{ 0, I_{\text{NH}} + I_\gamma - I_{\text{PU}} \right\} \right) / p_T^\ell \quad (1.6)$$

is used when selecting prompt leptons.

Isolation	$ \eta < 1.0$	$1.0 < \eta < 1.479$
I_{CH}	0.0360	0.0377
I_{NH}	0.0597	0.0807
I_{γ}	0.1210	0.1107
I_{CH}^{\max}	0.01064	0.1026

Table 1.1: Effective areas for isolations.

1.2 Particle Identification

1.2.1 Muons

The first step of the PF algorithm reconstructs three types of muon candidates: the standalone muons described in Section 1.1.6, outside-in global muons, and inside-out tracker muons. To construct a global muon, the algorithm identifies an inner track consistent with the trajectory of a standalone muon evolved inwards using a Kalman filter similar to those discussed in Section 1.1.1. After finding a match, a global muon candidate is created by combining the inner track with the standalone track with a second Kalman filter. Conversely, to construct a tracker muon, the algorithm identifies a muon segment consistent with the trajectory of a inner track with $p_T > 0.5 \text{ GeV}$. Global and tracker muons sharing the same inner track are merged into a single candidate. For muons with $p_T < 200 \text{ GeV}$, the muon momentum is that of the inner track, while the momentum is determined from a global fit of the muon chambers and inner tracker for muons with momentum above this threshold.

Hadrons misidentified muons are rejected through two separate mechanisms. First, the isolation with respects to inner tracks and calorimeter deposits within $\Delta R < 0.3$ is required to be less than 10% of the muon p_T . Non-isolated muons are kept only if certain selections on the reduced χ^2 of the track fit and the two impact parameters d_0 and d_z are satisfied. Finally, misidentified or misreconstructed muons can lead to a spurious imbalance in the transverse momentum. The procedure used to identify and remove these muon candidates is described in Section 1.2.6. The total efficiency of muon reconstruction is 99%.

The work described in this thesis only considers global muons with $p_T > 10 \text{ GeV}$

and $|\eta| < 2.5$. This minimum requirement is only used to reject events containing a muon and is referred to as the veto muon ID. The loose muon ID adds the requirement that the relative combined PF Isolation $I_{\text{PF}}^{\text{rel}}$ must be less than 0.25. must be less than 0.25. In order for a muon to pass the tight ID, it must have $p_T > 30 \text{ GeV}$ and $I_{\text{PF}}^{\text{rel}} < 0.15$ as well as satisfying the additional requirements in Table 1.2.

Variable	Selection	Description
$\chi^2_{\text{track fit}}/N_{\text{dof}}$	< 10	quality of global-muon track fit
$N_{\text{hit}}^{\mu\text{on}}$	> 1	at least one muon-chamber hit
$N_{\text{station}}^{\mu\text{on}}$	> 2	segments in at least two muon stations
d_0	$< 2 \text{ mm}$	reject cosmic ray muons
d_z	$< 5 \text{ mm}$	reject muons from pileup
$N_{\text{hit}}^{\text{pixel}}$	> 1	at least one pixel hit
$N_{\text{hit}}^{\text{tracker}}$	> 5	more than five tracker layers with hits

Table 1.2: Selections for the tight muon ID.

1.2.2 Electrons

Electron candidates are seeded from the GSF tracks described in Section 1.1.1 as long as the corresponding ECAL clusters are not linked to three or more additional tracks. In each block, all ECAL clusters linked to either the supercluster (SC) or one of the GSF track tangents are associated with the candidate to ensure optimal energy containment. Additional tracks linked to these clusters are associated if the track momenta and energies of any linked HCAL clusters are compatible with the electron hypothesis. Any tracks and clusters belonging to identified photon conversions linked to the GSF track tangents are associated as well.

To recover any energy lost during the association process, the total energy of the collected clusters is corrected with analytical functions of E and η . For ECAL-based candidates, the sum of the energies measured in the HCAL cells within $\Delta R < 0.15$ of the supercluster must be less than 10% of the supercluster energy. The final energy of an electron candidate is a weighted average of the corrected ECAL energy and the momentum of the GSF track and the electron direction is that of its GSF track.

The work described in this thesis only considers electrons with $p_T > 10 \text{ GeV}$ and $|\eta| < 2.5$. Additionally, electrons must pass further cuts on the observables listed in Table 1.3. The exact values of the cuts are tuned based on whether the electron is in the barrel or the endcap and to give desired signal efficiencies and background acceptance. The loose ID is tuned to 90% signal efficiency and 0.5% background acceptance, while the tight ID is tuned to 70% signal efficiency and 0.1% background acceptance.

Variable	Description
$\sigma_{inj\eta}$	energy-weighted cell width in the η -direction of the SC
$\Delta\eta$ and $\Delta\phi$	angular separation between the SC seed and the GSF track
H/E	energy ratio of the corresponding ECAL and HCAL towers
$I_{\text{PF}}^{\text{rel.}}$	relative combined PF Isolation
$ 1/E - 1/p $	difference between calorimeter energy and tracker momentum
$N_{\text{hit}}^{\text{miss}}$	number of missing hits in the inner tracker
Conversion veto	presence of tracks originating from a converted photon

Table 1.3: Variables used in selecting electrons.

1.2.3 Isolated Photons

Photon candidates are seeded from the ECAL superclusters (SCs) described in Section 1.1.4 as long as they have no links to GSF tracks and $E_T > 10 \text{ GeV}$. The same cluster and track association process described for electrons in Section 1.2.2 is used for photons, with the photon energy and direction being that of the final supercluster. This is motivated by the observation that the additional energy corrections used to improve the photon energy resolution cause photon candidates with large cluster width to exhibit unphysical energies. Figure 1-2 is a profile of the magnitude of the energy correction in bins of $\sigma_{inj\eta}$, the energy-weighted cell width in the η -direction.

As an illustration, an unphysically large correction is causing the transverse momentum of the photon object in the event shown in Fig. 1-3 to be nearly twice as large as the transverse momentum imbalance, which is supposed to balance the visible, i.e., photon momentum. Photon candidates with wide showers are used to estimate the hadron-to-photon misidentification background, while the photon energy resolution

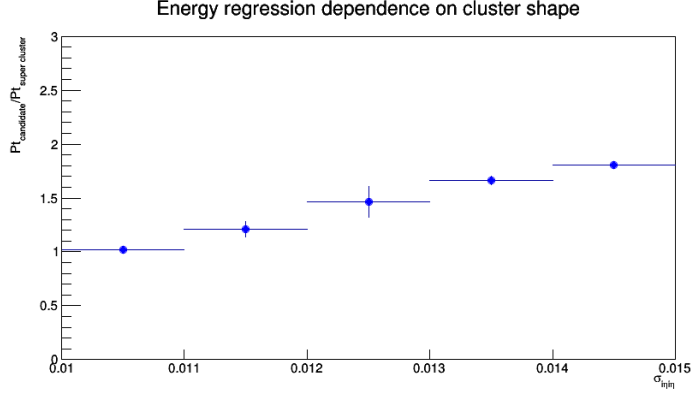


Figure 1-2: Magnitude of the energy correction on the photon object in bins of σ_{inj} .

has an insignificant effect. Therefore, the unbiased supercluster energy was chosen over the corrected photon energy.

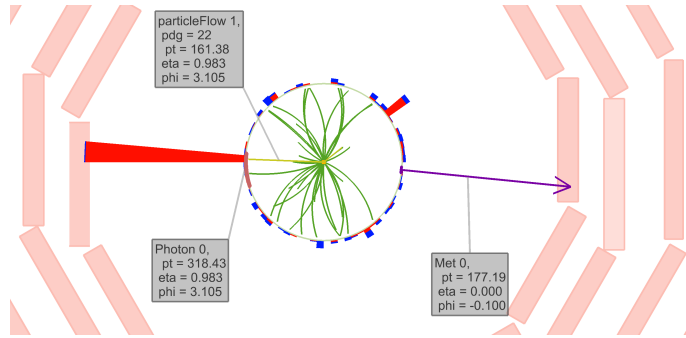


Figure 1-3: An example event where a photon with a wide shower receives a large energy correction.

For the work shown in this thesis, we are only concerned with high- E_T photons from the ECAL Barrel that have a supercluster with $E_T > 175 \text{ GeV}$ and $|\eta| < 1.4442$. To reduce hadron-to-photon misidentification rate, we apply the collection of isolation and shower shape selections in Table 1.4, which will hereby be referred to as the e/γ ID. To reject electrons from the candidate sample, no electron track seeds in the pixel detector can be associated to the supercluster. This is known as the pixel seed veto. To clean the candidate sample from photon objects originating from non-collision sources, we apply the collection of cuts shown in Table 1.5, which combined with the pixel seed veto constitutes the γ -specific ID. The beam halo tagger E_{MIP} is the total

energy deposited in ECAL by a hypothetical beam halo muon that passes through the photon cluster. See Section ?? for more detail on beam halo processes. The lower bounds on $\sigma_{in\eta\eta}$ and $\sigma_{i\phi i\phi}$ as well as the requirement on the cluster seed time $|t_{seed}|$ are employed to reject spurious photon objects arising from the “ECAL spikes” discussed in Section 1.3.2.

Variable	Maximum Value
H/E	0.0260
$\sigma_{in\eta\eta}$	0.01040
ρ -corrected I_{CH}^{\max}	1.146
ρ -corrected I_{NH}	$2.792 + 0.0112 \times E_T^\gamma + 0.000028 \times (E_T^\gamma)^2$
ρ -corrected I_γ	$2.176 + 0.0043 \times E_T^\gamma$

Table 1.4: Selections for the e/γ portion of the photon ID. Isolation values and E_T^γ are all in units of GeV.

Variable	Selection	Description
E_{MIP}	< 4.9 GeV	ECAL energy from a hypothetical beam halo muon
$\sigma_{in\eta\eta}$	> 0.001	non-trivial shower width in the η -direction
$\sigma_{i\phi i\phi}$	> 0.001	non-trivial shower width in the ϕ -direction
$ t_{seed} $	< 3 ns	timing of the cluster seed relative to bunch crossing

Table 1.5: Additional selections beyond the pixel seed veto for the γ -specific portion of the photon ID.

1.2.4 Hadrons

The last candidates reconstructed in a given block are the charged and neutral hadrons from fragmentation and hadronization, as well as the non-isolated muons and photons produced from their respective decays.

Inside the tracker acceptance of $|\eta| < 2.5$, all trackless HCAL clusters are reconstructed as neutral hadrons while all trackless ECAL clusters are reconstructed as photons. The preference towards photons is motivated because photons carry 25% of the jet energy and neutral hadrons do not interact strongly with the ECAL. Conversely, outside of the tracker acceptance, it is no longer possible to distinguish

charged and neutral hadrons, so any ECAL clusters linked to HCAL clusters are assumed to arise from unidentified charged hadrons. Thus, only unlinked ECAL clusters are reconstructed as photons and linked ECAL and HCAL clusters are reconstructed as neutral hadrons.

Afterwards, the only remaining PF elements are HCAL clusters linked to one or more tracks and ECAL clusters linked to one of these tracks. A single charged hadron is constructed for each remaining HCAL cluster, with energy equal to the sum of the ECAL and HCAL clusters and momentum equal to the sum of the individual track momenta.

If the energy of the charged hadron exceeds its momentum by an amount larger than the calometric energy resolution, neutral hadrons and photons are added. For excesses greater than 500 MeV, a photon with energy equal to the excess is created. If this photon cannot explain the entire excess, e.g. the excess is larger than the ECAL energy by at least 1 GeV, the remainder is identified as a neutral hadron. After photons and neutral hadrons consume the excess calometric energy, charged hadrons are constructed from the linked tracks with their energy and momentum determined by the track momenta under the charged-pion hypothesis.

If energy and momentum of the charged hadron are compatible, no neutral particles are identified. A charged hadron candidate is created for each track linked to the HCAL cluster, with momenta determined by a χ^2 fit of the tracker and calorimeter measurements. This combination ensures a smooth transition between the tracker-dominated low-energy regime and the calorimeter-dominated high-energy regime while always improving the final energy resolution.

If the momentum of the charged hadron exceeds its energy by three standard deviations, new PF muons are made from any non-isolated global muons failing the cleaning described in Section 1.2.1 with momentum resolution better than 25%. If, after masking the tracks from these muons, the track momentum sum still greatly exceeds the calorimeter energy, all remaining tracks with a p_T uncertainty greater than 1 GeV are identified, sorted in decreasing order of this uncertainty, and sequentially masked until no such tracks remain or the momentum excess disappears, whichever

comes first. At this point, the HCAL cluster is reconstructed according to one of the procedures defined in the preceding paragraphs.

When three or more charged particle candidates are linked to a secondary vertex identified as described in Section 1.1.3, a single primary charged hadron with energy equal to the sum of their energies replaces them in the reconstructed particle list. If an incoming track is associated with the vertex, it determines the direction of the primary charged hadron, which is otherwise determined by the vectorial sum of momenta of the secondary particles. If the momentum of the incoming track is well measured, the energy of undetected secondary particles is estimated and added to the energy of the primary charged particle.

1.2.5 Jets

As discussed in Section ??, jets are produced during the fragmentation and hadronization of colored particles produced in the hard scattering. After all PF candidates have been identified, a sequential recombination algorithm is used in an attempt to cluster these jets. Given an object i in the event E , we define the distance to the beam and the distance to another object j to be

$$d_{iB} = (p_T^i)^{2q} \quad \left| \quad d_{ij} = \min \left\{ (p_T^i)^{2q}, (p_T^j)^{2q} \right\} \frac{(\Delta R_{ij})^2}{R^2}, \right. \quad (1.7)$$

respectively, where q and R are tunable parameters and ΔR_{ij} is the angular distance between the two particles. The distance parameter R is an approximate measure of the cone size ΔR of the jet, while the power of the energy scale q defines the relationship between the relationship between the momentum and angular factors. Jets clustered with $q = -1$ are referred to as anti- k_T jets, those with $q = 0$ as Cambridge-Aachen jets, and those with $q = 1$ as k_T jets. Negative values of q force the clustering of circular jets around hard seeds ensuring that the resulting jet boundaries are resilient with respect to soft radiation. Within CMS, anti- k_T jets with $R = 0.4$ are used to cluster the parton shower from single partons.

The implementation in the FastJet library reduces the computational complex-

ity of clustering from $\mathcal{O}(N^2)$ to $\mathcal{O}(N \log N)$ for jets with hundreds or thousands of constituent particles. First, the two objects i and j with the smallest distance d_{ij} between them are found. If d_{ij} is less than both d_{iB} and d_{jB} , they are removed from E and a single object k with four-momentum $p_\mu^k = p_\mu^i + p_\mu^j$ which is added in their place. Otherwise if $d_{iB} < d_{jB}$, object i is removed from E and added to the set of jet candidates J while object j is kept, and vice versa if $d_{jB} < d_{iB}$. This procedure continues until all objects are removed from E and J contains all possible jet candidates.

1.2.6 Missing Tranverse Energy

The production of neutrinos and dark matter candidates produces a momentum imbalance in the transverse plane. The missing transverse momentum \vec{p}_T^{miss} is defined as the negative vectorial sum of all the PF candidates in the event E such that

$$\vec{p}_T^{\text{miss}} = - \sum_{i \in E} \left(\hat{x} \cdot p_T^i \cos \phi + \hat{y} \cdot p_T^i \sin \phi \right), \quad (1.8)$$

and its magnitude is the missing transverse energy $E_T^{\text{miss}} = |\vec{p}_T^{\text{miss}}|$. In a perfectly reconstructed event, non-zero E_T^{miss} implies the presence of neutrinos or DM candidates; however, the failure to properly reconstruct energy deposits or the reconstruction of PF candidates with incorrect energy results in events with large amount of fake E_T^{miss} .

One last cleaning of the PF candidates is conducted in an attempt to fix these events. To remove muons from cosmic rays, muon candidates with trajectories more than 1 cm away from the beam axis are removed if the measured E_T^{miss} is consequently reduced by half. For muons with $p_T > 20 \text{ GeV}$, the choice of subdetector used to estimate momemtum is reviewed and the smallest available estimate used if it reduces the measured E_T^{miss} by half. Additionally, the assignment of charged hadrons and neutral hadrons is reconsidered to ensure a charged hadron is not reconstructed as a muon and neutral hadron and vice versa.

Fake E_T^{miss} can persist in an event even after the final cleaning of PF candidates. At this point, events are checked against a known set of filters identifying possible sources of fake E_T^{miss} not captured by the PF algorithm. One set of filters is the HCAL

and ECAL filters that identify events with calorimeter clusters caused by noise from the shape and timing of the energy distribution. Another such filter is the beam halo filter that identifies energy deposits from muons produced from interactions between the beam and the machine that travel parallel to the beam. These muons are identified by their localization in ϕ and a longitudinal track left in the ECAL endcaps and the CSCs. Applying these filters removes essentially all remaining events with fake E_T^{miss} while rejecting less than 1% of events with real E_T^{miss} .

1.3 Reconstruction Issues

This thesis focuses on events with a single high- p_T photon and large E_T^{miss} . There are a lot of reconstruction issues specific to this final state as photons are relatively easy to fake through other processes that result in a large amount of fake E_T^{miss} . This section describes the three main sources of correlated fake photons and fake E_T^{miss} encountered during this analysis.

1.3.1 ECAL gain-switch effect

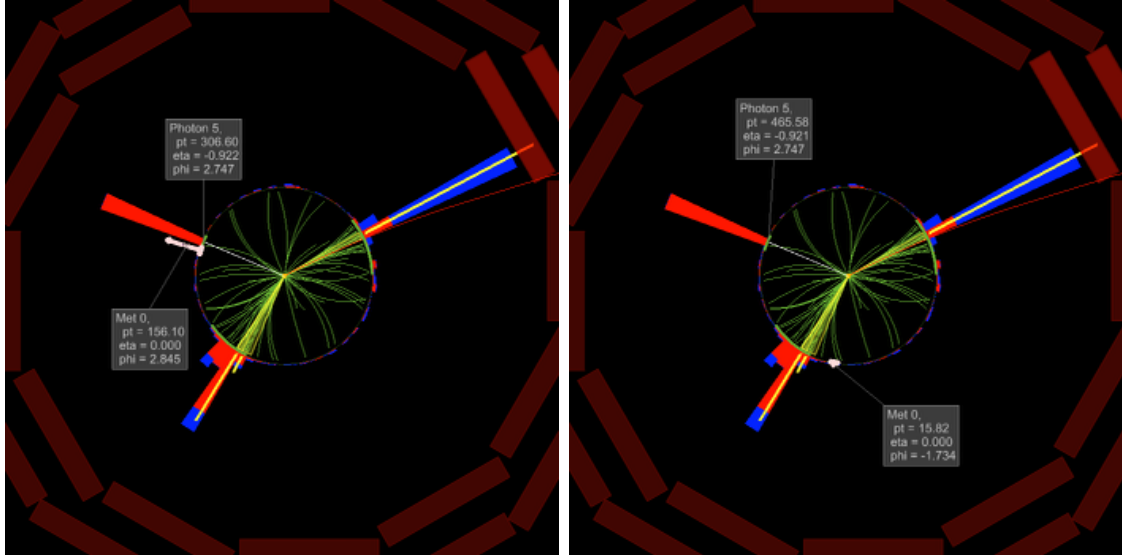


Figure 1-4: Two event displays comparing the same event, reconstructed without (left) and with (right) the fix for ECAL gain-switch effect.

The “multi-fit” algorithm for ECAL hit reconstruction was found to have an unexpected behavior when there is a large energy deposit onto a single ECAL crystal, such that the electronic signal converted at the frontend electronics is sourced partially from channels of the preamplifier with lower gains (6 or 1) than the default (12) channel. In the most dramatic cases, pulse misreconstruction would result in underestimation by hundreds of GeV of photon p_T . This effect is mitigated in the reprocessed data set used for this analysis by identifying ECAL clusters whose seed crystal hit had a switch of gains, and performing an alternative pulse reconstruction when possible.

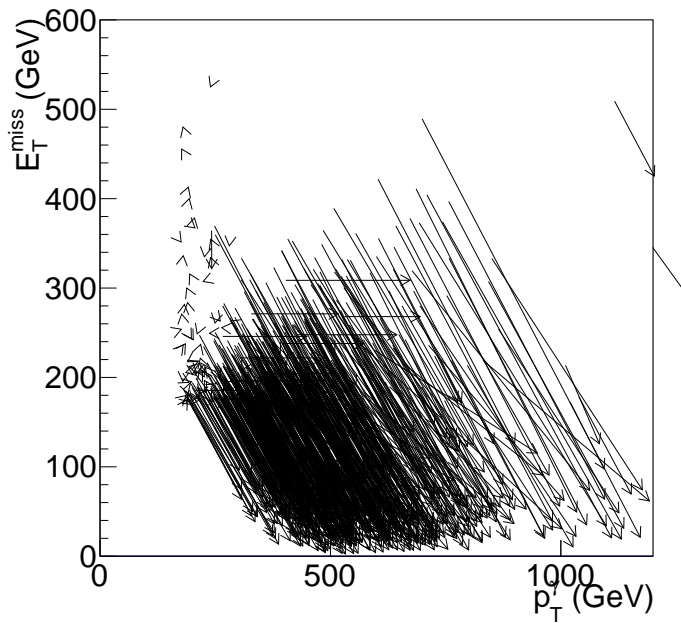


Figure 1-5: The change in reconstructed photon p_T and E_T^{miss} for events in the bin $\Delta\phi(\gamma, p_T^{\text{miss}}) < 0.05$ of the distribution in Figure ???. Each arrow represents a single event, the the tail (head) of the arrow corresponding to $(E_T^\gamma, E_T^{\text{miss}})$ coordinates in the datasets without (with) the fix for the gain-switch problem.

The gain-switch problem affected the analyses documented in this thesis, since large underestimation of the energy of a photon in an otherwise typical $\gamma + \text{jets}$ event would introduce large missing transverse momentum to the event, typical collinear to the affected photon. Figures 1-4 and 1-5 are the visualization of how the new dataset changes the reconstructed photon energy and E_T^{miss} .

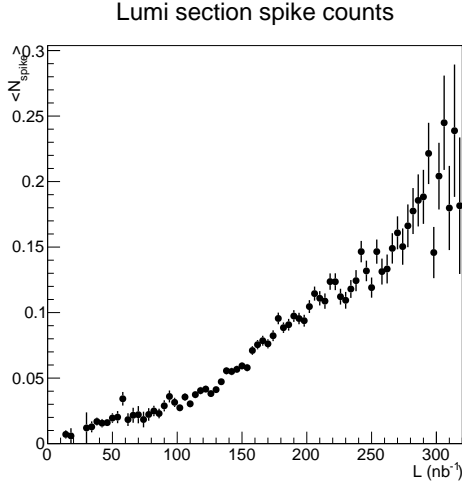


Figure 1-6: Average number of spike clusters in a luminosity section, identified by $\sigma_{in\eta\eta} < 0.001$ and $E > 50$ GeV, in muon-triggered events, versus integrated luminosity of the luminosity section.

1.3.2 ECAL Barrel Spikes Phenomenology

Noise in the photodetector or the detector electronics can result in spurious photon signals. Most of the time, such spurious signal is filtered out by multiple layers of protection, starting from the so-called “spike killer” algorithm at the Level 1 trigger [?]. Nevertheless, in rare cases, noise in a single ECAL channel coincides with pileup or other energy deposit in the nearby crystals and appear as a high-energy photon cluster.

The origin of ECAL spikes is believed to be interactions of neutrons and other hadronic particles (collectively called neutral hadrons hereafter) with the photocathode material of the ECAL avalanche photo diodes (APD). Nuclear fission at the APD surface then causes a large electron avalanche, which is mistaken as a large photon yield scintillation in the ECAL crystal. Evidences supporting this hypothesis is documented in Ref. [?]. In Figure 1-6, scaling of the rate of spikes with the instantaneous luminosity is confirmed, up to much higher luminosity values than was observed at the time when Ref. [?] was written.

A known feature of such spurious photon clusters is that the recorded pulse shape of the seed crystal, i.e., the channel with the noise, is not what is expected from a

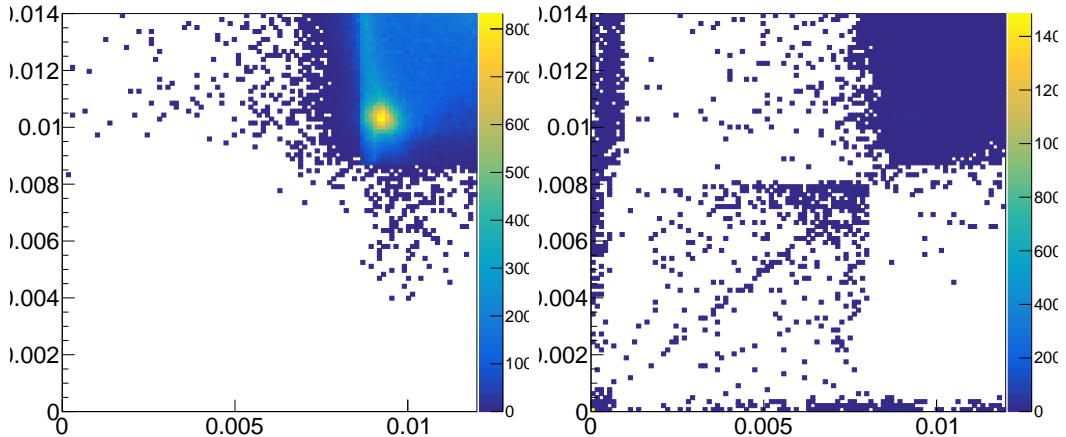


Figure 1-7: Two-dimensional distributions in $\sigma_{i\phi i\phi}$ and $\sigma_{i\eta i\eta}$ of ECAL clusters in the standard reconstruction (left) and the special reconstruction with no spike cleaning (right).

real electromagnetic shower in ECAL. In particular, this translates to a distinctive early rec hit time distribution, since the rec hit time is extracted from a fit to the pulse shape assuming a normal pulse.

In the normal CMS data reconstruction, rec hits that are tagged as spike-like are ignored in clustering. Rec hits are tagged as spikes if there is very little energy deposit recorded in the surrounding crystals, or if the reconstructed time is out of an allowed window. Identical algorithms are employed in the HLT and offline reconstructions.

To study an unbiased spike sample, ECAL DIGI samples stored in the SingleMuon AOD datasets are reconstructed into ECAL clusters with no spike cleaning applied. DIGIs associated with the standard and “uncleaned” photon objects are stored in AOD, and ones for the uncleaned photons is rich in spike-like hits. Figure 1-7 shows how narrow clusters are cleaned away in the normal reconstruction.

Figure 1-8 shows the spacial and temporal distributions of the rec hits seeding narrow ($\sigma_{i\eta i\eta} < 0.001$) clusters. The spacial distribution appears mostly random, indicating that there is no single source of spike-like rec hits. The two highest peaks in the time distribution at $t \sim -15$ ns and $t \sim 10$ ns are characteristic of pulse shapes, which rise faster than the pulse from the normal scintillation. The second peak is

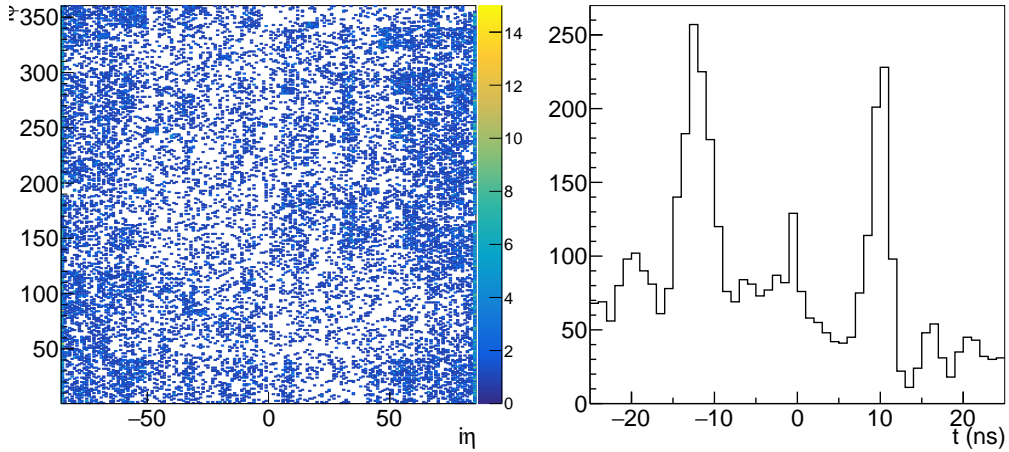


Figure 1-8: $\eta-\phi$ and time distributions of seed hits of narrow ($\sigma_{i\eta i\eta} < 0.001$) clusters.

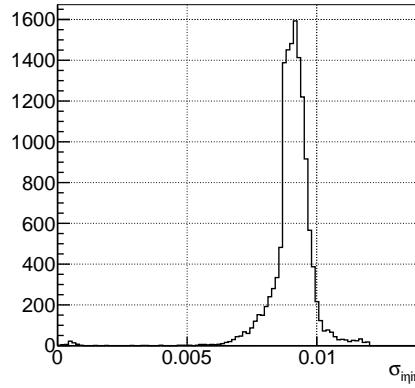


Figure 1-9: $\sigma_{i\eta i\eta}$ distribution of uncanceled clusters from $\gamma+\text{jets}$ MC simulation.

understood to come from the next bunch crossing.

The small peak at $t \sim 0$ in the time distribution of Fig. 1-8 is due to actual “physical” clusters that happened to have a very narrow cluster shape. By processing the $\gamma+\text{jets}$ MC simulation events through this special reconstruction, we see that about 0.5% of ECAL clusters from prompt photons have $\sigma_{i\eta i\eta} < 0.001$ as shown in Figure 1-9.

To understand the time distribution, one can investigate the original DIGI samples from which rec hits are made. At each event readout, a single ECAL channel outputs 10 ADC signals corresponding to a sampling of the analog pulse output of multi-gain

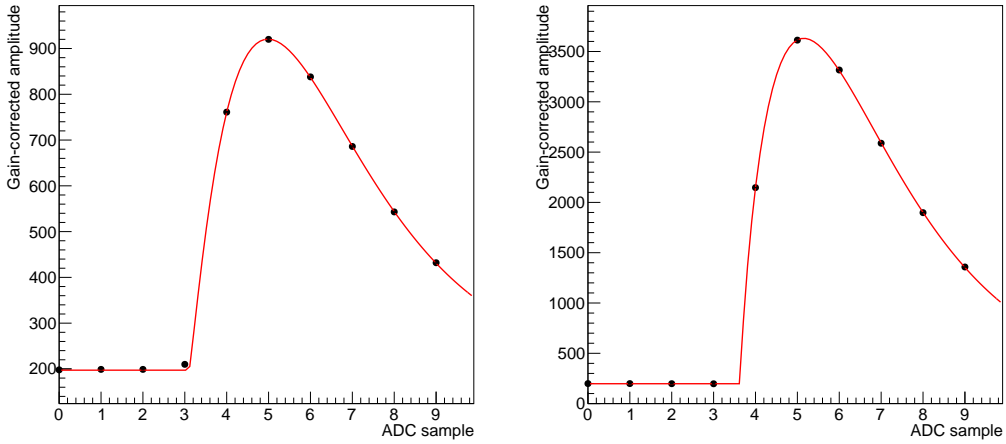


Figure 1-10: Example ECAL DIGIs and corresponding pulse shapes reconstructed through χ^2 fits of Equation 1.9, for normal (left) and spike-like (right) hits.

preamplifier (MGPA) in range $t_0 - 125 \text{ ns} < t < t_0 + 100 \text{ ns}$, where t_0 is the time of the triggering bunch crossing. These 10 signal points can be described well by the formula

$$f(t) = A \left(1 - \frac{t - \tau}{\alpha\beta}\right)^\alpha \exp\left(-\frac{t - \tau}{\beta}\right). \quad (1.9)$$

In the formula, parameters A and τ correspond to the pulse amplitude and peak time, whereas α and β control the shape of the pulse. Figure 1-10 illustrates various observed pulse shapes fit with the above formula with all parameters floating. A χ^2 fit is employed using the average noise amplitude of each MGPA channel as the errors on the data points. The noise is measured in ECAL calibration cycles in the inter-fill period and is recorded in the conditions database.

In the α - β parameter space, seed rec hits of wide clusters concentrate around $(\alpha, \beta) \sim (1.1, 1.7)$, while spike-like hits populate the region $\alpha < 0.9$ as shown in Figure 1-11. In fact, the pulse amplitude distribution of narrow-cluster seeds with $\alpha > 0.9$ is unlike that of the narrow-cluster seeds with $\alpha < 0.9$, and resembles the amplitude distribution of wide-cluster seeds shown in Figure 1-12. This suggests that the population $\alpha > 0.9$ correspond to the clusters of physical, prompt photons. It

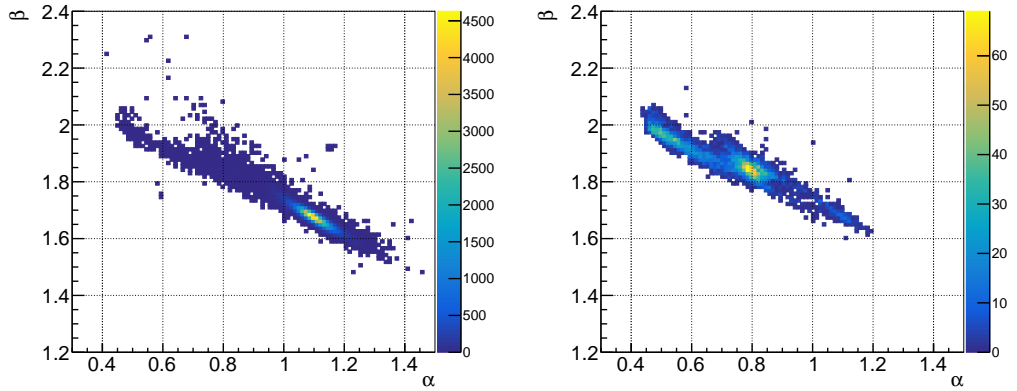


Figure 1-11: α - β distributions of the seed hits of physical wide clusters (left) and spike-like clusters (right).

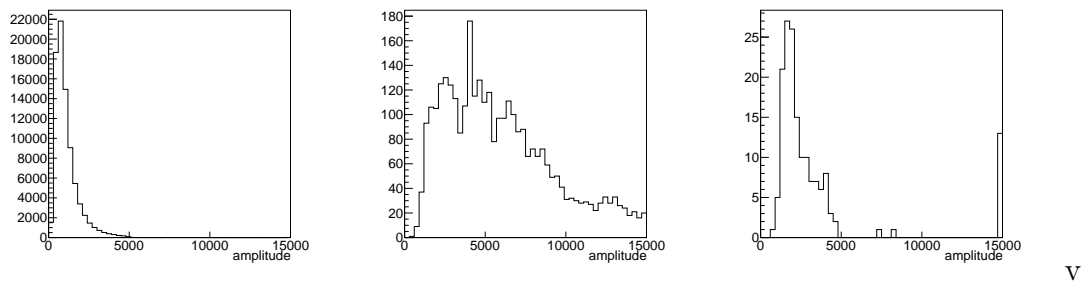


Figure 1-12: Seed crystal pulse amplitude distributions of physical wide clusters (left), narrow clusters with $\alpha < 0.9$ (center), and narrow clusters with $\alpha > 0.9$ (right).

then follows that spike hits can be regarded to exclusively have sharp pulse shapes.

Chapter 2

The Monophoton Analysis

In this chapter, we discuss the search for dark matter produced in association with a single high- p_{T} photon. Our benchmark signal models are the vector and axial dark matter mediators discussed previously. However, many Standard Model (SM) processes are also capable of producing events with a single high- p_{T} photon and large $E_{\mathrm{T}}^{\mathrm{miss}}$, whether with real photons, other particles misidentified as photons, or unphysical photon signatures from various machine and detector processes.

The most significant are the irreducible backgrounds, where the underlying physics process produces the exact same signature as the signal with only real and properly identified physics objects. In this case, the irreducible backgrounds are the associated production of a high-energy γ with either a Z boson that subsequently decays to a pair of neutrinos or a W boson that decays to a charged lepton and a neutrino, with the charged lepton outside of the detector acceptance. These two processes are denoted as $Z(\rightarrow \nu\bar{\nu})+\gamma$ and $W(\rightarrow \ell\nu)+\gamma$, respectively, and together they account for approximately 70% of the SM background, with 50% from the former and 20% from the latter. The modeling of the irreducible backgrounds is explained in Section 2.6.

Additional backgrounds arise from events where the candidate photon object is a misidentified electron (Section 2.4) or an electromagnetic shower caused by hadrons (Section 2.5). The background events from electron misidentification are mostly W boson production ($W \rightarrow e\nu$), whereas those from hadron misidentification are due to multiple sources such as $Z(\rightarrow \nu\nu) + \text{jets}$ and QCD multijets with grossly mismea-

sured jet energy. Misidentification itself is rare, but because these processes have high cross sections, the amount of background is substantial, approximately 15% and 5% respectively. Since object misidentification rates depend on subtle details of the detector, the MC simulation often fails to accurately describe them. Therefore, the contributions from these background processes are estimated by employing data-driven techniques, where the misidentification rates are measured in data and applied to proxy samples with well-identified electrons or hadrons.

Finally, apparent large energy deposits in ECAL from non-collision processes mimic $\gamma+E_T^{\text{miss}}$ events and therefore need to be controlled. Known sources of such background include bremsstrahlung of beam halo or cosmic ray muons and anomalous ECAL energy deposits resulting from the interaction of particles in the ECAL photodetectors referred to as “ECAL spikes”. These methods used to estimate contributes from these processes are described in detail in Sections 2.7 and 2.8, respectively.

The estimates of the contributions from $Z(\rightarrow \nu\bar{\nu})+\gamma$, $W(\rightarrow \ell\nu)+\gamma$, and beam halo processes are allowed to float in the fits to data performed to extract the potential signal contribution and set limits on new physics models. Meanwhile, for all other background processes, the yields in the fits are fixed to the estimates from data-driven methods or MC cross section calculation.

2.1 Dataset

The data sample was collected with a single-photon trigger: `HLT_Photon165_HE10`. This high-level trigger algorithm is relatively simple, only requiring at least one photon candidate with $E_T > 165 \text{ GeV}$ reconstructed with a corresponding L1 seed. The photon candidate must also have $H/E < 0.1$ to discriminate against jets, where H/E is the ratio of HCAL to ECAL energy deposits in the central calorimeter tower corresponding to the candidate. The photon energy reconstructed at the HLT is less precise relative to that derived later in the offline reconstruction. Therefore, the online thresholds in the trigger on both H/E and E_T^γ are less restrictive than their offline counterparts.

The trigger efficiency is measured to be about 98% for events passing the analysis selection with $E_T^\gamma > 175$ GeV and the integrated luminosity of the analyzed data sample is $(35.9 \pm 0.9) \text{ fb}^{-1}$ [?].

2.1.1 Trigger Efficiency

We measure the trigger efficiency by looking for trigger objects that match the candidate photon object in an appropriate data set because the trigger decisions are based on the existence of a single photon object in the event. A trigger object is the four-momenta of an object reconstructed at the trigger level that is used for making trigger decisions. A trigger object is matched to the candidate when their angular separation $\Delta R = \sqrt{\Delta\eta^2 + \Delta\phi^2}$ is less than a certain threshold. For the photon candidate object, a line that connects the detector origin and the cluster position was used to define its direction because photons leave no tracks and do not bend in the magnetic field.

The trigger efficiency measurement is performed on the SingleMuon data set, exploiting events mostly from leptonic $t\bar{t}$ ($e\mu$) topology. Events with a candidate-quality photon without the pixel seed veto requirement and a muon object that passes the “tight” identification requirement and matches the trigger object of the HLT_IsoMu24 or HLT_IsoTkMu24 triggers are used. The matching rate of the photon object and the trigger object is the trigger efficiency. Figure 2-1 shows the L1+HLT combined efficiency as a function of the photon E_T . It can be seen that the trigger is fully efficient for $E_T > 175$ GeV.

For the first period of data taking, the HLT_Photon165_HE10 trigger was seeded only by an isolated e/γ L1 trigger. This L1 seed becomes inefficient at high E_T due to a misconfiguration in the H/E computation algorithm as indicated by the drop in efficiency at high- E_T shown in the left side of Figure 2-2. To mitigate the effect, in the later periods, the trigger was seeded by the logical **OR** of SingleEG40 and SingleJet L1 triggers, combining multiple with various p_T thresholds.

Even with this addition, the measured trigger efficiency is not 100% at the plateau, but it is flat with respect to E_T as shown on the right of Figure 2-2. In principle,

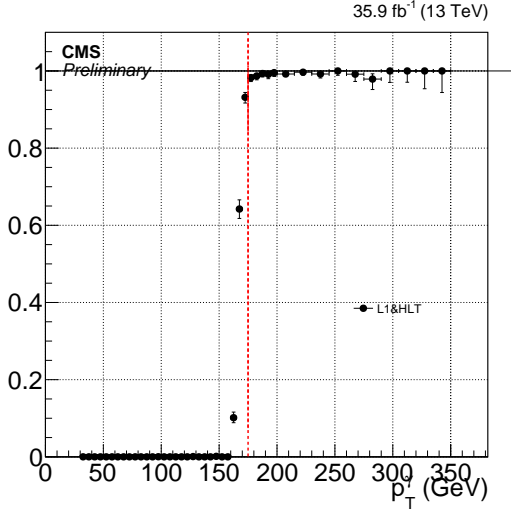


Figure 2-1: The efficiency turn-on of the `HLT_Photon165_HE10` trigger for photons passing the candidate selection, measured using $\mu + e/\gamma$ events from the SingleMuon data set. Red vertical line corresponds to $E_T = 175$ GeV.

the efficiency should be applied to all simulation-based background estimates whose normalization is fixed by theoretical calculation of the cross section. However, the only simulation-based background processes with absolute normalization are those that contribute at $\mathcal{O}(1)\%$, with large systematic uncertainties. Therefore we deem the slight discrepancy of the trigger efficiency from unity as irrelevant.

2.1.2 Pileup Reweighting

The distribution of the number of pileup interactions inserted into MC events differ from the true pileup distribution, estimated from the measurement of instantaneous luminosity, beam intensity of each proton bunch, and the total cross section of proton inelastic scattering (69.2 mb^{-1}).

Figure 2-3 shows the pileup distributions in data and MC and their ratio. Each simulation event has its weight multiplied by the value of the ratio evaluated at the number of true pileup interaction injected into the event.

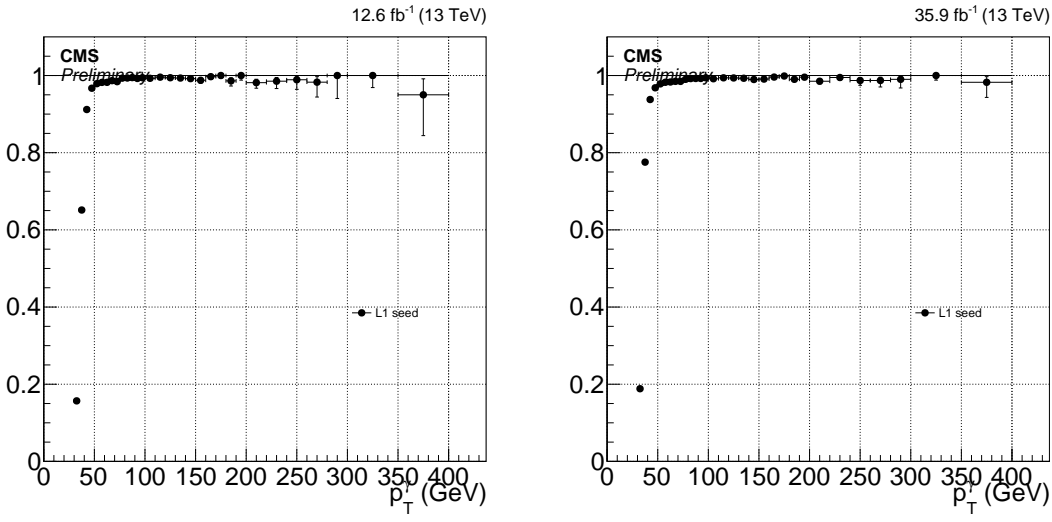


Figure 2-2: The efficiency of the L1 seed for the signal trigger in periods B and C (left) and the full data set (right). The drop in efficiency at high- E_T in the earlier period is fixed by the addition of SingleJet L1 seeds during the remainder of data-taking.

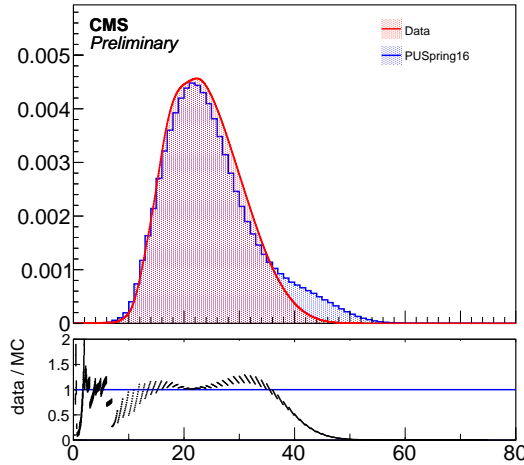


Figure 2-3: The pileup distributions in data and MC.

2.2 Event Selection

From the recorded data, events are selected by requiring $E_T^{\text{miss}} > 170 \text{ GeV}$ and at least one photon with $E_T^\gamma > 175 \text{ GeV}$ in the fiducial region of the ECAL barrel ($|\eta| < 1.44$). Events with photons in the endcaps are not considered because the estimate of backgrounds due to beam halo and misidentified hadron are greatly complicated due to the x - y grid of the crystals in the endcaps.

Events with a high- p_T photon and large E_T^{miss} are subjected to further requirements to suppress SM background processes that feature a genuine high-energy photon, but not a significant amount of E_T^{miss} . One such SM process is $\gamma + \text{jets}$, where an apparently large E_T^{miss} is often the result of mismeasuring the energy of a jet. In contrast to signal-like processes, the E_T^{miss} is typically smaller than E_T^γ in these events, so requiring the ratio of E_T^γ to E_T^{miss} to be less than 1.4 rejects this background effectively with little effect on signal efficiency. Events are also rejected if the minimum opening angle between \vec{p}_T^{miss} and the directions of the four highest p_T jets, $\min\Delta\phi(\vec{p}_T^{\text{jet}}, \vec{p}_T^{\text{miss}})$, is less than 0.5. Only jets with $p_T > 30 \text{ GeV}$ and $|\eta| < 5$ are considered in the $\min\Delta\phi(\vec{p}_T^{\text{jet}}, \vec{p}_T^{\text{miss}})$ calculation. In the $\gamma + \text{jets}$ process, rare pathological mismeasurements of E_T^γ also lead to large E_T^{miss} . For this reason, the candidate photon \vec{p}_T and \vec{p}_T^{miss} must be separated by more than 0.5 radians.

Variable	Selection	Motivation
E_T^γ	$> 175 \text{ GeV}$	high- p_T photon passing trigger
$ \eta $	< 1.44	region with best background estimates
E_T^{miss}	$> 170 \text{ GeV}$	characteristic signature of dark matter
$E_T^\gamma/E_T^{\text{miss}}$	< 1.4	reduce jet mismeasurement backgrounds
$\min\Delta\phi(\vec{p}_T^{\text{jet}}, \vec{p}_T^{\text{miss}})$	< 0.5	reduce jet mismeasurement backgrounds
$\Delta\Phi(\vec{p}_T^\gamma, \vec{p}_T^{\text{miss}})$	> 0.5	reduce photon mismeasurement backgrounds

Table 2.1: Baseline selections for all events considered in the analysis.

The above selections, summarized in Table 2.1, constitute the baseline selections common to all regions. To improve the purity of the signal region, we require a more stringent photon identification as well as additional object vetos. The contributions from the $Z(\rightarrow \nu\bar{\nu}) + \gamma$ and $W(\rightarrow \ell\nu) + \gamma$ processes to the signal region are modeled

by fitting to observed data in control regions where one or two leptons (electrons or muons) are identified in addition to the photon candidate while the contributions from misidentified electrons and hadrons are modeled by proxy regions where some of the selections in the photon identification have been inverted. The additional requirements for the various signal, control, and proxy regions used in the analysis are described in the following sections.

2.2.1 Signal Regions

The defining feature of the signal region is the application of both the e/γ and γ -specific portions of the photon ID, given in Tables 1.4 and 1.5 respectively. The former reduces the hadron misidentification rate with a collection of isolation and shower shape selections while the latter reduces the electron misidentification rate with the pixel seed veto and rejects non-collisions backgrounds with specifically tailored selections.

In the signal region, events are vetoed if they contain an electron or a muon with $p_T > 10 \text{ GeV}$ that is separated from the photon by $\Delta R > 0.5$. This lepton veto rejects SM processes that produce a high- p_T photon, E_T^{miss} , and leptons such as $W(\rightarrow \ell\nu) + \gamma$, $t\bar{t}\gamma$, and $VV\gamma$.

Furthermore, to constrain the beam halo normalization, the signal region is split into two parts according to the variable ϕ' introduced in Equation 2.9. The region defined by $|\phi'| < 0.5$ is called the horizontal region, its complement $0.5 < |\phi'| < \pi/2$ is called the vertical region, and the two together are referred to as the combined signal regions.

2.2.2 Control Regions

The single-electron (single-muon) control region is defined by requiring exactly one tight electron (muon) with $p_T > 30 \text{ GeV}$ and $|\eta| < 2.5$ (2.4) in addition to requiring the same photon ID as in the signal regions. To suppress the contributions from large- E_T^{miss} processes other than $W(\rightarrow \ell\nu) + \gamma$, the transverse mass $m_T =$

$\sqrt{2E_T^{\text{miss}} p_T^\ell [1 - \cos \Delta\phi(\vec{p}_T^{\text{miss}}, \vec{p}_T^\ell)]}$ must be less than 160 GeV. Additionally, for the single-electron control region, E_T^{miss} must be greater than 50 GeV to limit the contribution from the $\gamma + \text{jets}$ process, where a jet is misidentified as an electron.

The dielectron (dimuon) control region is defined by exactly two electrons (muons) in addition to the photon, with $60 < m_{\ell\ell} < 120$ GeV, where $m_{\ell\ell}$ is the mass of the dilepton system. The leading lepton must pass the tight ID requirements, while the trailing lepton only needs to pass the loose ID requirements.

Finally, in the control regions, the recoil vector $\vec{U} = \vec{p}_T^{\text{miss}} + \sum_\ell \vec{p}_T^\ell$ serves as an analogue for the \vec{p}_T^{miss} in the signal region. In the signal region, the \vec{p}_T^{miss} is a proxy for the vector boson p_T while in the control regions, the recoil vector is used instead. Thus, the recoil \vec{U} must satisfy identical requirements to those for the \vec{p}_T^{miss} in the signal region to keep the control region kinematics as similar as possible to the signal region kinematics.

2.2.3 Proxy Samples

To estimate the background due to misidentified electrons, an electron proxy sample is used. This proxy sample is obtained by identical event selection as that of the signal region but with the pixel-seed veto inverted on the photon candidate object. Such a photon candidate is referred to as an electron proxy object. This yields a sample of events with similar kinematics to the signal region and well-identified electron candidates, differing only from the misidentified electron events in that a pixel hit was associated with the photon object. Thus, these exact events are used to estimate the misidentified electron background after scaling them by the electron-to-photon misidentification rate.

To estimate the background due to misidentified hadrons, a hadron proxy sample is used. This proxy sample is obtained by identical event selection as that of the signal region but where the photon candidate passes the e/γ and γ -specific IDs with exception for at least one of the following cuts: $\sigma_{inj} < 0.01022$ and $I_{\text{CH}} < 0.441$ GeV. Such a photon candidate is referred to as a hadron proxy object. This yields a sample of events with similar kinematics to the signal region and well-identified proxies for

misidentified hadrons. Thus, these exact events are used to estimate the misidentified hadron background after scaling them by the hadron-to-photon misidentification rate.

Additional tight and loose hadron proxy objects and samples are made by tightening and loosening the constant term in the I_{NH} and I_{γ} requirements on the proxy object. The specific values for each proxy object are shown in Table 2.2.

	I_{NH} (GeV)	I_{γ} (GeV)
Nominal	2.792	2.176
Loose	10.910	3.630
Tight	0.264	2.362

Table 2.2: Constant terms in the I_{NH} and I_{γ} selections for the hadron proxy objects.

2.2.4 Measurement Samples

To measure the photon purity and part of the photon efficiency, an EM object+jet measurement sample is formed by requiring an EM object with $E_{\text{T}} > 175 \text{ GeV}$ and $|\eta| < 1.44$ plus at least one jet with $p_{\text{T}} > 100 \text{ GeV}$ and $|\eta| < 2.5$ which passes the loose jet ID. An EM object is a photon candidate that passes the e/γ ID with the exception of the following relaxed cuts: $\sigma_{i\eta i\eta} < 0.015$ and $I_{\text{CH}} < 11.0 \text{ GeV}$. Additionally, we apply an $E_{\text{T}}^{\text{miss}} < 60 \text{ GeV}$ cut to make this region orthogonal to the signal region.

To measure the hadron misidentification rate, a hadron proxy+jet measurement sample is formed by replacing the the EM object in the EM object+jet sample with a hadron proxy object, one for each type of hadron proxy. These are exactly the same as the hadron proxy samples, except that a high- p_{T} jet has replaced the high- $E_{\text{T}}^{\text{miss}}$, minimizing the kinematic differences between the two.

2.3 Photon ID Efficiency Scalefactor

While we try to model the CMS detector as accurately as possible with our MC simulations, there are still differences between the behavior of photons within the simulations and those from data taken with the detector. Most importantly, this

results in different efficiencies for photons in data dn MC, which we must measure. To improve our MC, we reweight it by the ratio of the efficiency in data to that in MC, known as the photon efficiency scalefactor.

When measuring the photon efficiency scale factor, we factorize the photon ID-into the e/γ portion and the γ -specific portion. The e/γ portion of the ID consists of a collection of isolation and shower shape selections designed to reduce the hadron misidentification rate. We measure the efficiency of the e/γ portion using the “tag-and-probe” (TP) method with $Z \rightarrow ee$ events as these variables have similar efficiencies for physical electrons and photons. The γ -specific portion of the ID consists of the pixel seed veto and non-collision rejection cuts. We measure the efficiency of γ -specific portion on a sample of physical photons in the EM object+jet measurement sample using a $\sigma_{inj\eta}$ template fit method.

We perform both efficiency estimates as a function of p_T with the binning [175,200], [200,250], [250,300], [300,350], [350,400] and $[400, \infty)$. This binning was chosen based on the number of available events in data for the failing probes fit in the TP method and the background template for the $\sigma_{inj\eta}$ fits, as these samples are the smallest and drive the uncertainty of the methods.

2.3.1 e/γ ID Efficiency

The efficiency corresponding to the e/γ part of the photon ID is estimated by exploiting Z boson decays into pairs of electrons and positrons. Using the TP method, a high-quality electron object (tag) is identified in a single photon data sample, and the accompanying electron is sought for in the pool of electromagnetic objects (probes) in the event. The area under the peak in the mass distribution of the tag-probe system around the Z boson mass (between 81 GeV and 101 GeV) is then measured once applying the $e\gamma$ ID requirements on the probe and once inverting all of the requirements simultaneously. Denoting the two areas under the peaks in the passing and failing

samples N_{pass} and N_{fail} , respectively, the resulting efficiency $\epsilon_{e/\gamma}$ is given by

$$\epsilon_{e/\gamma} = \frac{N_{\text{pass}}}{N_{\text{pass}} + N_{\text{fail}}}. \quad (2.1)$$

The TP measurement is performed on a subset of the single photon triggered events where there is an electron object (tag) passing the “tight” identification criteria in addition to the triggering photon (probe). All possible tag-probe combinations are considered; if the tag object can also serve as a probe and the probe object as a tag, which is a common occurrence in the case when the probe is electron-like (passes the $e\gamma$ ID), then the two combinations are considered independently to avoid the bias caused by preferring to use one object over another as the probe.

The tag-probe mass distributions are then fit to extract N_{pass} and N_{fail} . The fit model is composed of two templates, where one template describes a pure $Z \rightarrow ee$ line shape and the other describes the background contributions. The backgrounds to the fits include $W+\text{jets}$, diboson, and $t\bar{t}$ productions, which are all negligible and estimated to contribute by less than 1%. Minor contributions from processes that do not involve true electrons, such as diphoton production with a strongly asymmetric conversion on one of the photons and misidentification of a QCD jet as an electron, are predicted to be negligible from MC studies.

The $Z \rightarrow ee$ template shape is an analytic convolution of the Breit-Wigner distribution and the Crystal Ball function. The mass and width parameters of the Breit-Wigner distribution are fixed to PDG values while the Crystal Ball parameters are allowed to float in the fit. We are able to use the analytic Breit-Wigner distribution instead of a template taken from MC because at this high probe p_T scale the selected events are mostly of the $Z+\text{jets}$ topology with a boosted Z boson. This makes the selection rather inclusive in terms of the tag-probe invariant mass and ensures that the Breit-Wigner distribution accurately models the mass distribution even through the tag and probe are under kinematically exclusive selections.

The background template is taken from events collected by the single photon trigger where an additional muon object is present, making use of the fact that the

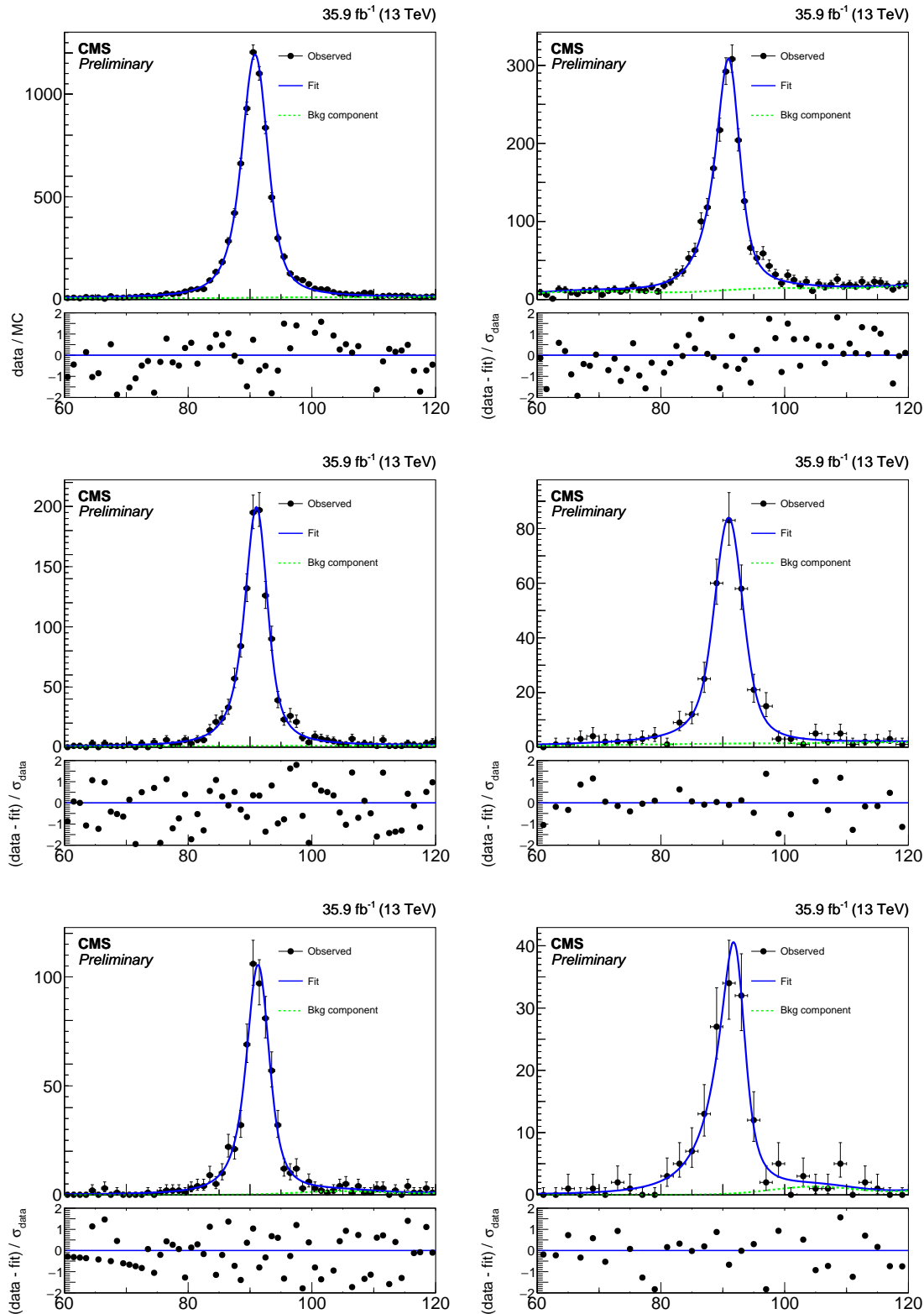


Figure 2-4: Fits to the mass distributions for pass (left) and fail (right) selections, in bins of probe p_T : $175 < p_T < 200 \text{ GeV}$ (top), $300 < p_T < 350 \text{ GeV}$ (middle), $p_T > 400 \text{ GeV}$ (bottom). The blue solid line represents the full fit model, and the green dashed line its background component.

most of the background processes in both fits are symmetric in lepton flavor. In order to mitigate statistical fluctuations in the background sample, the actual template is constructed by a Gaussian kernel estimation of the mass distribution of this muon-probe sample.

The floating parameters of the fits are therefore the normalizations of the $Z \rightarrow ee$ and background templates and the Crystal Ball smearing parameters. Selected example fits are shown in Figure 2-4.

The statistical uncertainty of the fits is estimated by generating toy data from the nominal fit result with the same number of entries as the fit target distribution. The mass distribution of the toy data is then fit with the same model with the parameters floating. This procedure is repeated 100 times to obtain a distribution of the $Z \rightarrow ee$ event yields, and its standard deviation is taken as the statistical uncertainty of the fit. Relative statistical uncertainty on the efficiency is 10%.

To estimate the effect of potential mismodeling in the fits, alternative fits varying the background and signal templates are performed first. In the alternative-background fit, a simple linear function is tested. In the alternative-signal fit, no Crystal Ball convolution is performed to the signal template and the mass and width of the Breit-Wigner function are allowed to vary. Resulting best-fit distributions of these alternative models are then used to generate a large number of toy distributions, which are fit by the nominal model. The average shift of the fit result from the nominal value is then taken as the uncertainty. The relative uncertainty on the efficiency varies from 2 to 4% depending on the probe p_T bin.

The MC efficiency is taken from counting the number truth-matched electrons passing and failing the e/γ part of the ID from a $Z \rightarrow ee$ sample. Additionally, the MC efficiency is computed using the same procedure as in data as a cross-check. The efficiencies obtained from these two methods are consistent within their uncertainties.

The data efficiencies, MC efficiencies, and resulting scale factors as a function of p_T are shown in Figure 2-5. The scalefactors are consistent with unity within the uncertainties. The numerical values are given in Table 2.3. We use the bin by bin scale factor corresponding to the truth values in the analysis.

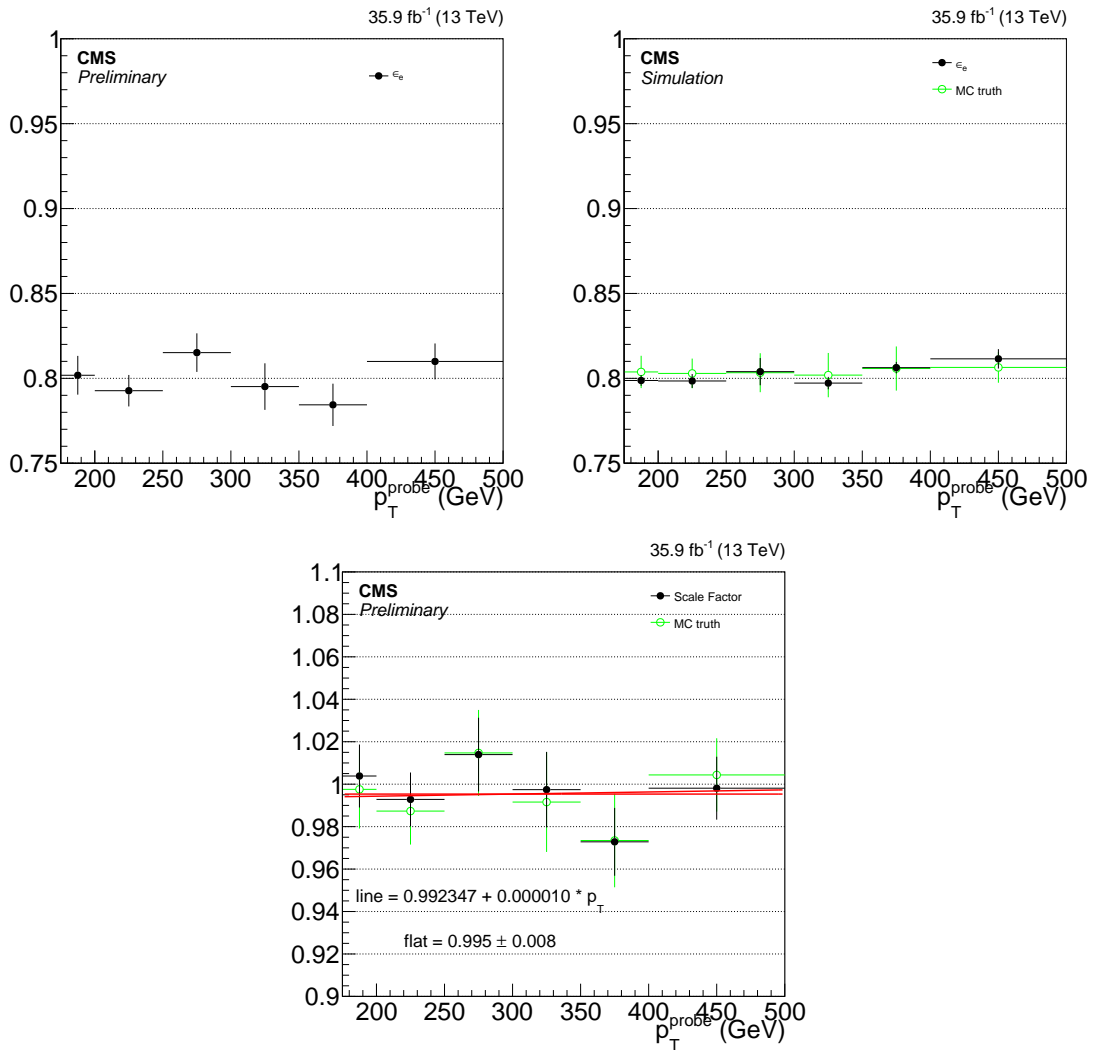


Figure 2-5: e/γ component of the photon identification efficiency for data (top-left) and MC (top-right) and corresponding scale factor (bottom) as a function of photon p_T .

p_T^{probe} (GeV)	MC Fit	Truth
(175, 200)	1.014 ± 0.008	1.009 ± 0.016
(200, 250)	1.003 ± 0.008	0.999 ± 0.014
(250, 300)	1.014 ± 0.010	1.016 ± 0.019
(300, 350)	1.002 ± 0.014	0.997 ± 0.022
(350, 400)	0.986 ± 0.012	0.987 ± 0.022
(400, 6500)	0.988 ± 0.011	0.999 ± 0.016

Table 2.3: e/γ scale factors as a function of photon p_T .

2.3.2 γ -specific ID Efficiency

To measure the efficiency of the γ -specific component of the photon ID, we use a $\sigma_{inj\eta}$ template fit to extract the number of true photons from a pool of photon objects passing the e/γ ID.

The measurement is performed using the EM object+jet measurement sample. We fit the $\sigma_{inj\eta}$ distribution of the EM object with a template describing the $\sigma_{inj\eta}$ shape of true photons and another describing the hadronic background. The real photon template is taken from γ +jets MC requiring the photon to pass the e/γ ID except for the $\sigma_{inj\eta}$ requirement. The fake photon template is taken from the same data control sample, requiring $5 \text{ GeV} < I_{\text{CH}} < 7 \text{ GeV}$. The number of true photons in the target sample is the integral of the post-fit real photon template below $\sigma_{inj\eta} = 0.0104$, the same value as in our photon ID.

The fit is performed once for all EM objects and then once for EM objects passing the γ -specific ID criteria. The ratio of the numbers of true photons obtained in the two fits is the efficiency.

The $\sigma_{inj\eta}$ template fit method in its simplest form fits the observed distribution with the following fit function:

$$P(f; \sigma_{inj\eta}) = f \cdot h_s(\sigma_{inj\eta}) + (1 - f) \times h_b(\sigma_{inj\eta}), \quad (2.2)$$

where h_s is the signal template, h_b is the background template, and f is the fraction of true photons in the target sample. Both the target template and the fit function are normalized to unity, removing the number of photon candidates in the target sample N as a fit parameter and leaving f as the only free parameter.

However, the hadronic background template, taken from the data control sample, has contributions from real photons with a I_{CH} value exceeding the ID requirements. The amount of this “photon contamination” depends on the sideband choice, but is non-zero even for a sideband with very large I_{CH} . As described below, we perform additional fits with the background templates from alternative sidebands $3.5 \text{ GeV} < I_{\text{CH}} < 5 \text{ GeV}$ (“near”) and $7.5 \text{ GeV} < I_{\text{CH}} < 9 \text{ GeV}$ (“far”) to assess the systematic

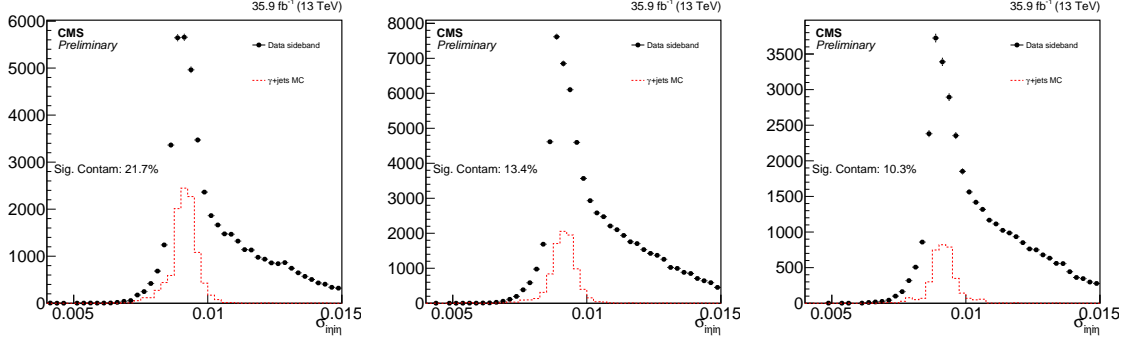


Figure 2-6: Signal contamination in the [3.5,5.0] (left), [5.0,7.5] (middle), and [7.5,9.0] (right) isolation sidebands.

uncertainty. The photon contamination of the nominal and far sideband is 10-15%, and in the near sideband, it can go up to approximately 20% (see Figure 2-6).

To remove the photon contamination from the background templates, we start with the true photon shape in the sideband $h_{s'}$, which differs from the signal template h_s in the I_{CH} selection applied to the photons. Then, we create a new background template h_b^{sub} from the original background template h_b by subtracting $h_{s'}$. After normalization to unity, we obtain the expression

$$h_b^{\text{sub}}(\sigma_{i\eta i\eta}) = \frac{h_b(\sigma_{i\eta i\eta}) - S'/B \cdot h_{s'}(\sigma_{i\eta i\eta})}{1 - S'/B}, \quad (2.3)$$

where B is the number of photon candidates in the sideband and S' is the number of true photons in the sideband.

To determine S' , we start with the number of true photons in the target sample, $f \cdot N$. We then scale this by the ratio of the relative fractions of true MC photons in the I_{CH} sideband r_{sb} and in the signal region r_{sig} , giving us the expression

$$S' = f \cdot \frac{r_{\text{sb}}}{r_{\text{sig}}} \cdot N. \quad (2.4)$$

Going back to our original fit function and replacing h_b with h_b^{sub} gives us

$$P(f; \sigma_{i\eta i\eta}) = f \cdot h_s(\sigma_{i\eta i\eta}) + (1 - f) \times \frac{h_b(\sigma_{i\eta i\eta}) - S'(f)/B \cdot h_{s'}(\sigma_{i\eta i\eta})}{1 - S'(f)/B}, \quad (2.5)$$

which converges to the original fit function if $S' = 0$, i.e., if there is no photon contamination in the sideband. Note that f is still the only free parameter for this new function as S' only depends on f and $r_{\text{sb}}/r_{\text{sig}}$ is set constant in the fit (see discussion of systematics for more detail).

There are four main sources of systematic uncertainty for this measurement. The first comes from the sideband choice, as the relative rates of different types of fake photons varies with I_{CH} . The second comes from the true photon I_{CH} shape, as this is used to determine the normalization of true photons in the sideband. Currently, this shape is taken from MC and thus there is the potential to mismodel the effects of the underlying event and pile-up. The third comes from the true photon $\sigma_{i\eta i\eta}$ distribution. As we take this from MC as well, we can mismodel the signal template shape. Finally, at high p_{T} , we suffer from low yields in our I_{CH} sidebands, which leads fluctuations that negatively influence the fit.

The uncertainty due to sideband choice is the larger of the differences of the purities measured using the near and far sidebands versus the nominal sideband. Figure 2-7 shows fits using the three sidebands for the $[175, 200]$ p_{T} bin on the left and for the $[400, \infty)$ p_{T} bin on the right.

To measure the uncertainty due to the I_{CH} shape, we look at the I_{CH} for electrons in $Z \rightarrow ee$ events in both data and MC. Using these distributions, we obtain a data/MC scale factor which we apply to the MC true photon I_{CH} distribution to obtain a scaled MC distribution. Then, we recount the photons using this new distribution and take the difference in the values obtained using the raw MC and scaled MC distributions as a systematic uncertainty.

To measure the uncertainty due to the signal template $\sigma_{i\eta i\eta}$ shape, we look at the $\sigma_{i\eta i\eta}$ distributions for electrons from $Z \rightarrow ee$ events in both data and MC. Using these distributions, we obtain a data/MC scale factor which we apply to the MC true photon $\sigma_{i\eta i\eta}$ distribution to obtain a scaled MC distribution. Then, we recount the photons using this new distribution and take the difference in the values obtained using the raw MC and scaled MC distributions as a systematic uncertainty.

To estimate the uncertainty due to statistical fluctuations in our background tem-

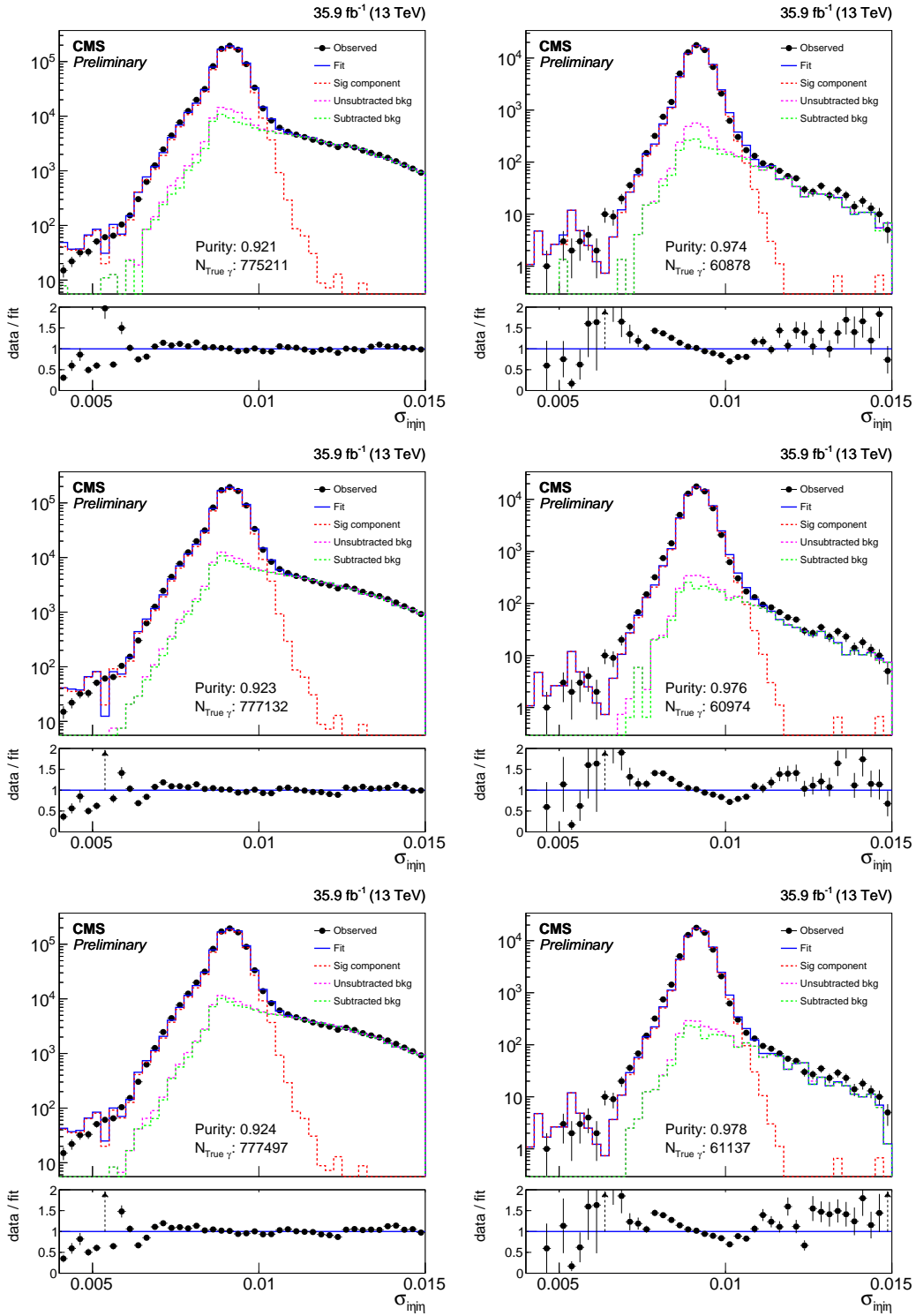


Figure 2-7: Fits to the $\sigma_{\text{inj}\eta}$ distributions for the $[175, 200]$ (left) and $[400, \infty)$ (right) p_T bins using the $[3.5, 5.0]$ (top), $[5.0, 7.5]$ (middle), and $[7.5, 9.0]$ (bottom) isolation sidebands. The blue solid line represents the full fit model, the red dashed line its signal component, and the green dashed line its background component.

plates, we generate toys from the background template from data. We then repeat the fit with each of these toys and plot the distribution of the difference between the purity value obtained from the toy templates versus the nominal template. We take the standard deviation of this distribution as a systematic uncertainty.

The values obtained for each systematic uncertainty on the true photon count of the denominator are shown in Table 2.4 in bins of p_T . The relative uncertainties on the numerator are similar, and in the efficiency, each uncertainty source is considered as fully correlated.

p_T Range (GeV)	Sources of Systematic Uncertainty				
	Sideband	I_{CH}	Shape	Signal Shape	Bgkd. Stats
(175, 200)	0.09	0.18	0.05	0.04	
(200, 250)	0.01	0.16	0.06	0.03	
(250, 300)	0.14	0.16	0.06	0.05	
(300, 350)	0.12	0.16	0.07	0.08	
(350, 400)	0.23	0.11	0.05	0.10	
(400, ∞)	0.27	0.09	0.05	0.05	

Table 2.4: Relative uncertainties on the estimated number of true photons in the denominator sample.

The MC efficiency of the γ -specific ID is determined by counting the number of truth-matched photons passing the e/γ part of the ID and the full ID. However, there is a complication, the γ +jets region in data has approximately 5% contamination from electrons before applying the pixel veto, as shown in Figure 2-8. To replicate this effect in the MC, we combine appropriately cross-section weighted γ +jets, W +jets, and $t\bar{t}$ samples and truth match to both electrons and photons. Additionally, to account for the NLO cross-section ratio uncertainties with respect to γ +jets at this p_T range, we apply a 14% uncertainty on the W +jets and $t\bar{t}$ yields, where the specific value comes from the uncertainty on the γ +jets to W +jets ratio in the monojet analysis [1]. This uncertainty is uncorrelated between the numerator and denominator as a negligible amount of electron events survive the pixel veto.

The data efficiency, MC efficiency, and the scale factor for the γ -specific ID as a function of p_T are shown in Figure 2-9. As there is no significant trend in the scale

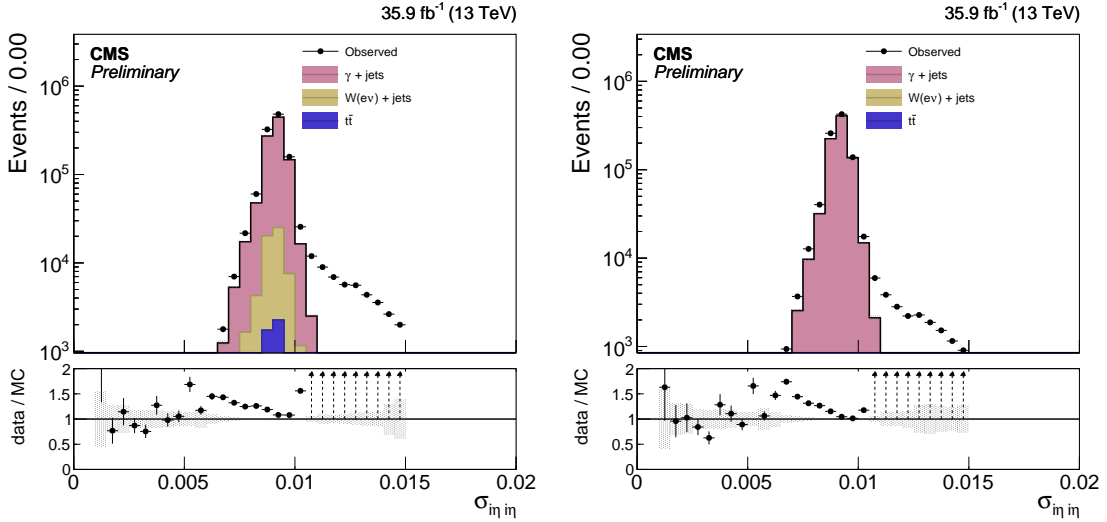


Figure 2-8: Electron contamination in $\gamma + \text{jets}$ region before (left) and after (right) applying the pixel seed veto.

factor as a function of p_T , we apply a flat scale factor of 0.9840 ± 0.0090 for all of the MC-based background and signal models in the analysis.

2.4 Misidentified electrons

An electron can be misidentified as a photon if the association of tracks or track seeds to the ECAL supercluster fails in the reconstruction step. The production of a single W boson decaying to an electron and a neutrino is a high-rate process, and it mimicks the photon plus E_T^{miss} signature if the electron is misidentified.

The rate at which this misidentification occurs is $R_e = (1 - \epsilon_e^{\text{track}})/\epsilon_e^{\text{track}}$, where $\epsilon_e^{\text{track}}$ is the tracking efficiency of electrons passing the photon identification criteria except for the electron veto. After making the reasonable assumption that the kinematic and other critical properties of the electron plus E_T^{miss} events are unaffected by the electron misidentification, we model the electron misidentification background by taking the electron proxy sample and scaling it by R_e .

We measure the factor R_e in data using the TP method described in Section 2.3.1 with changed definitions for passing and failing probes and an adjustment to the

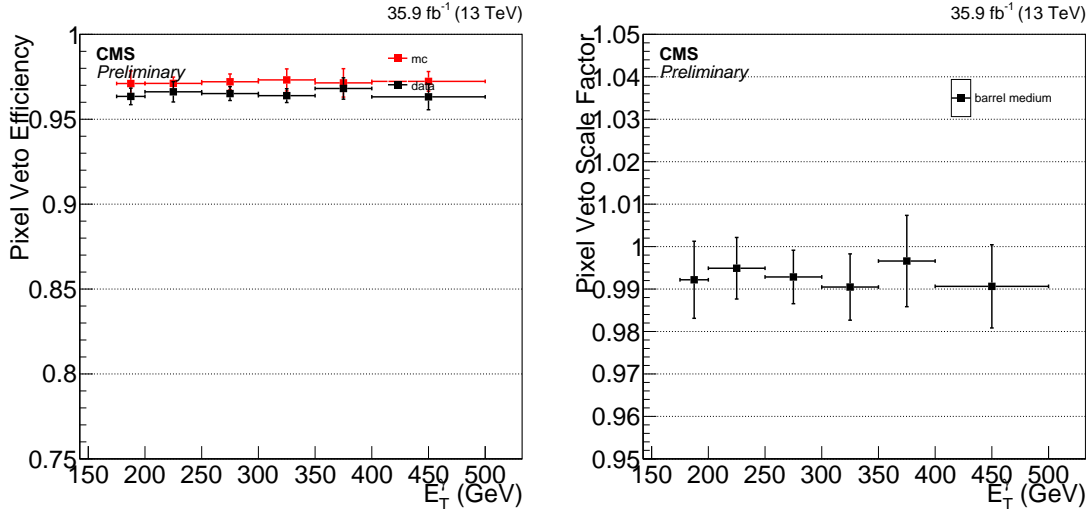


Figure 2-9: Photon pixel veto efficiencies (left) and corresponding scale factor (right) as a function of photon p_{T} .

background model. The ee category contains passing probes with a pixel seed while the $e\gamma$ category contains failing probes without a pixel seed. Probes in both categories must pass the remainder of the e/γ and γ -specific IDs. Denoting the area of the peak in each category N_{ee} and $N_{e\gamma}$, respectively, the ratio $N_{e\gamma}/N_{ee}$ is equal to R_e up to minor systematic corrections.

Additionally, the backgrounds to the $e\gamma$ fit consist of processes with an electron and an actual photon in the final state, such as $W\gamma$ and $Z \rightarrow ee$ with a hard radiation off one of the electrons. To account for the higher rate of bremsstrahlung experienced by electrons than by muons, we scale the mass distribution of the $\mu + \gamma$ sample by the ratio of electron-probe to muon-probe events taken from MC. As an alternative template to assess the systematic effect introduced by the choice of the background template, the unscaled mass distribution is also tested.

Figure 2-10 shows the six fits performed on ee and $e\gamma$ in bins of probe p_{T} , from which the R_e factor used for the estimation of the electron misidentification background is derived. Figure 2-11 shows the derived R_e factor as a function of E_{T}^{γ} . The electron proxy sample is reweighted by R_e depending on the p_{T} of the electron proxy object.

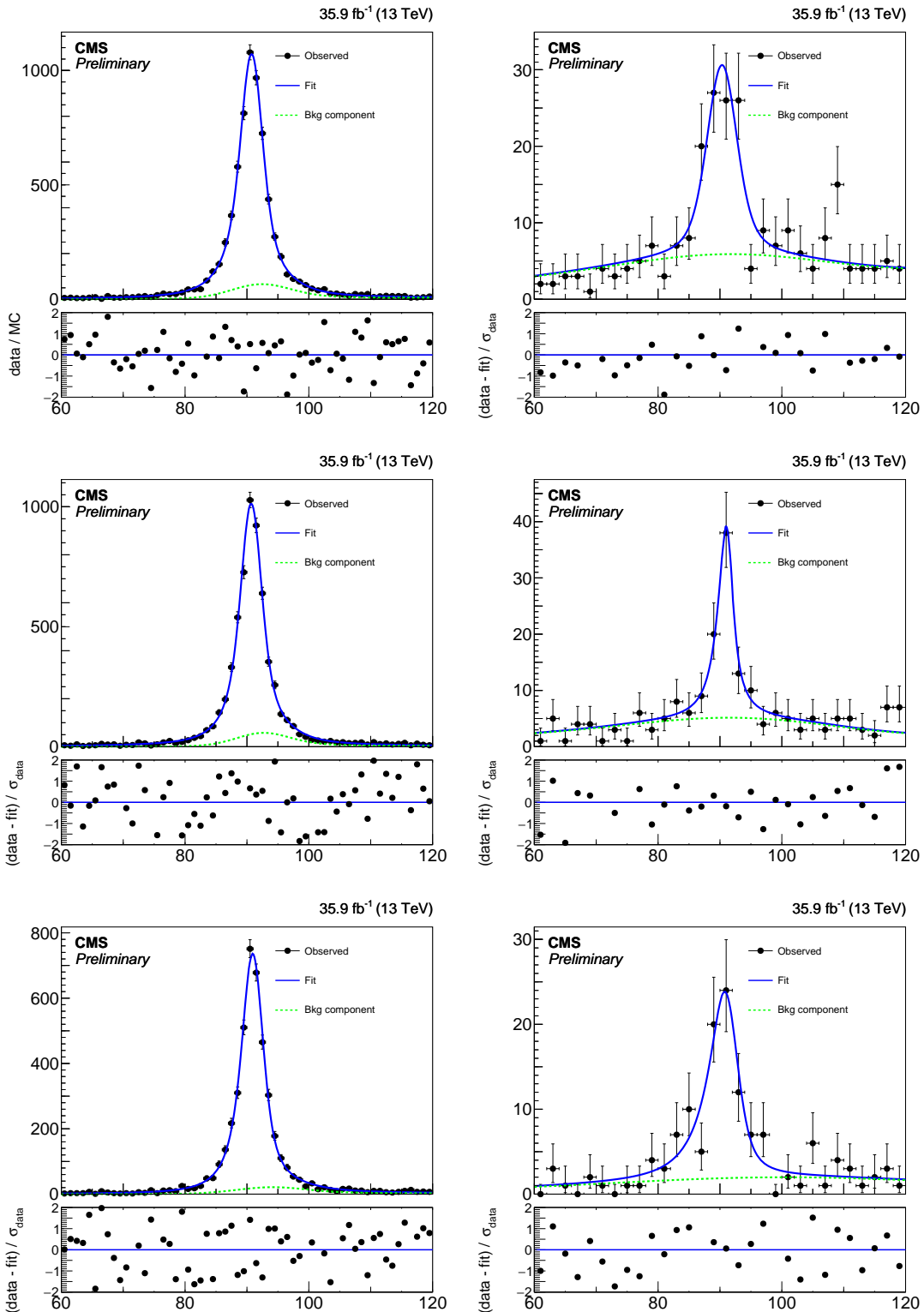


Figure 2-10: Fits to the mass distributions for ee (left) and $e\gamma$ (right) selections, in bins of probe p_T : $175 < p_T < 200$ GeV (top), $200 < p_T < 250$ GeV (middle), $p_T > 250$ GeV (bottom). The blue solid line represents the full fit model, and the green dashed line its background component.

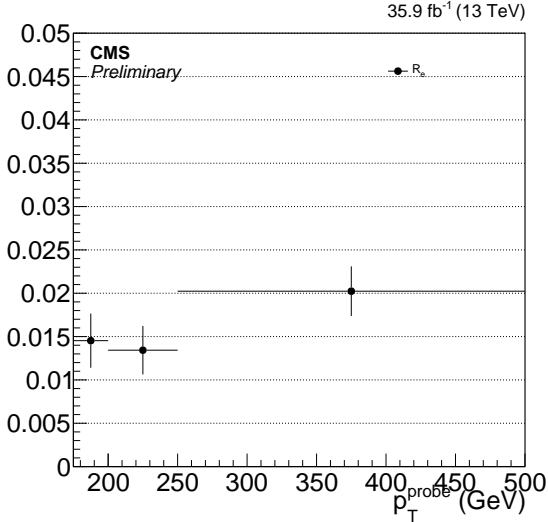


Figure 2-11: Electron to photon fake rate R_e .

2.5 Misidentified hadrons

A hadron can be misidentified as a photon if fragmentation processes results in mainly neutral hadrons that subsequently decay to collimated pairs of photons. The production of $Z + \text{jets}$ where the Z boson decays to neutrinos is a high-rate process, and it mimicks the photon plus E_T^{miss} signature if the hadrons from the jet are misidentified.

Without the presence of additional charged tracks or neutral hadron energy deposits, the only way to distinguish these EM-like hadrons from real photons is through the shower shape. Thus, we measure the fraction of hadronic objects within a pool of photon candidate objects in the EM object+jet measurement sample using the $\sigma_{i\eta j\eta}$ template fit method from Section 2.3.2. Figure 2-12 and Table 2.5 show the final impurity and associated uncertainties as a function of p_T .

The hadronic transfer factor R_h measures the rate at which hadronic proxy objects result in hadrons that are misidentified as candidate photons. The factor R_h is obtained by dividing the estimated number of misidentified hadrons in the EM object+jet measurement sample by the number of events in the hadron proxy+jet measurement sample as a function of p_T . Figure 2-13 shows the transfer factor R_h along with the various distributions used for its derivation.

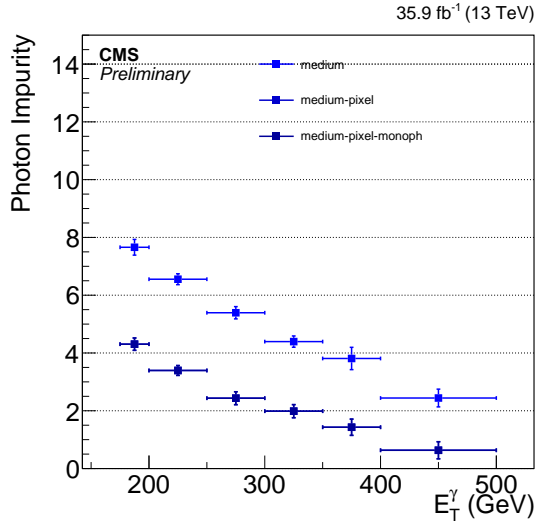


Figure 2-12: The percent impurity for photons as a function of p_T . The different bands show the effects of adding different stages of the full ID, starting with the e/γ portion of the ID and successively adding the pixel seed veto followed by the rest of the γ -specific portion of the ID. These last two curves overlap, as the non-collision rejection cuts do not effect the rate at which hadrons are misidentified as photons.

p_T (GeV)	Nominal	Sources of Systematic Uncertainty				
		Sideband	CH	Iso Shape	Signal Shape	Bgkd. Stats
(175, 200)	4.31 ± 0.21	0.09	0.18	0.05	0.04	
(200, 250)	3.39 ± 0.17	0.01	0.16	0.06	0.03	
(250, 300)	2.44 ± 0.22	0.14	0.16	0.06	0.05	
(300, 350)	1.99 ± 0.23	0.12	0.16	0.07	0.08	
(350, 400)	1.43 ± 0.28	0.23	0.11	0.05	0.10	
(400, ∞)	0.63 ± 0.30	0.27	0.09	0.05	0.05	

Table 2.5: Impurities for photons as a function of p_T .

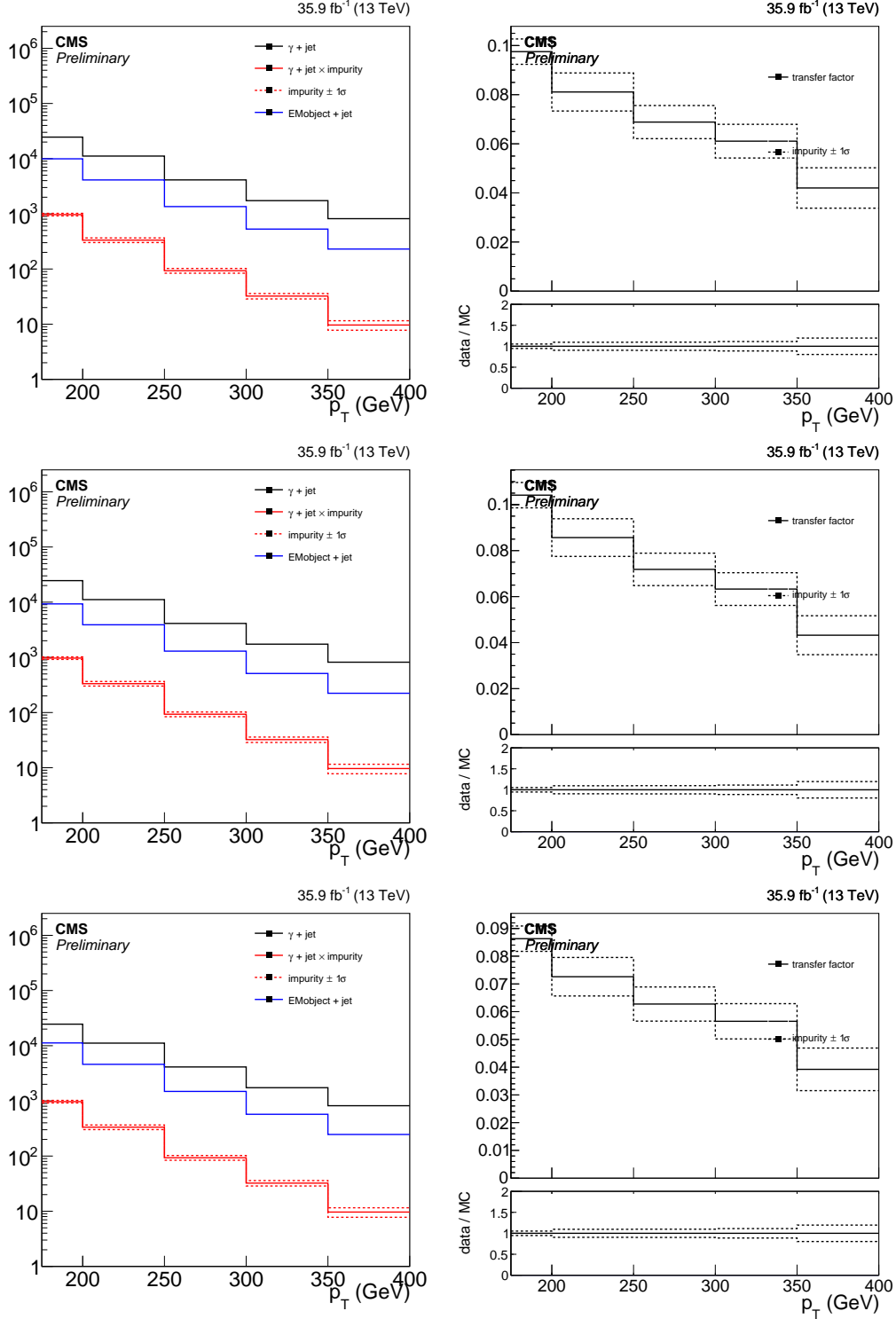


Figure 2-13: Left: The p_T distribution of the candidate photon object in the photon + jet control sample (black), the result of scaling it with the impurity (red), and the p_T distribution of the hadronic proxy object in the proxy + jet control sample (blue). Right: Hadronic transfer factor R_h , which is the ratio of the red and blue distributions in the left plot. Top: Nominal hadron proxy object. Middle: Tighter hadron proxy object. Bottom: Looser hadron proxy object.

Under the assumption that the R_h stays constant regardless of whether the event has a high- p_T jet or E_T^{miss} , the hadron proxy sample is weighted by R_h to determine the number of events due to misidentified hadrons in the signal region.

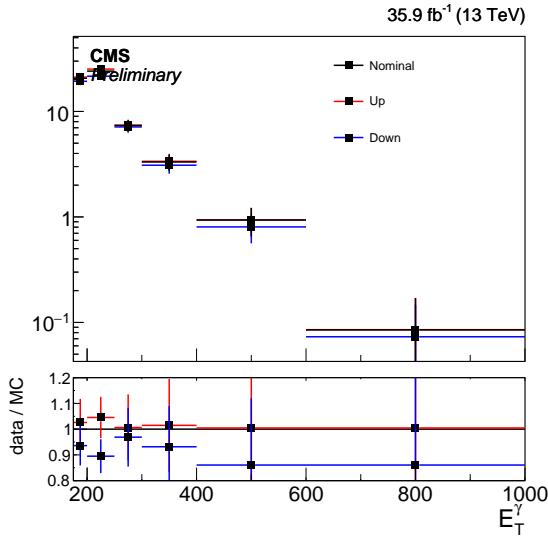


Figure 2-14: The p_T distribution of the estimated contribution from hadronic fakes in the signal region. The distribution labeled Up (Down) comes from the tighter (looser) selection. The systematic uncertainty resulting from this variation is around 5% at the low end of our p_T range and increases to 15% after $p_T > 400$ GeV.

To estimate the uncertainty on this background, we repeat the above method using additional proxy and measurement samples with tighter and looser definitions of the hadron proxy object. The different distributions from the nominal, tight, and loose selections are shown in Figure 2-14. The tight and loose shapes are taken as the one sigma band around the nominal estimate. Additionally, there is an uncertainty coming from the estimation of the photon purity. Figure 2-15 shows the resulting shapes from moving the shapes generated by a one sigma shift in the purity.

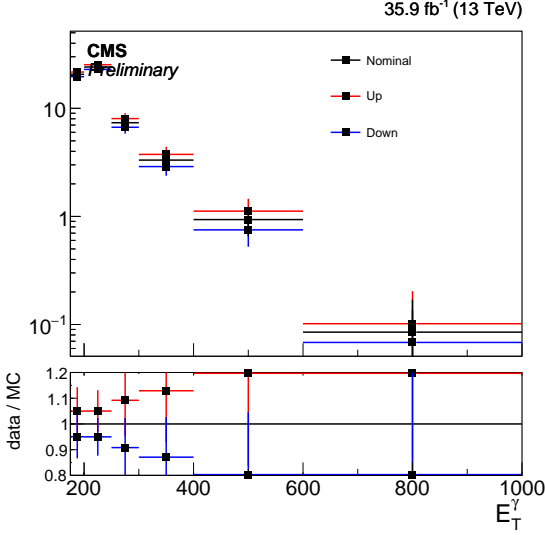


Figure 2-15: The p_T distribution of the estimated contribution from hadronic fakes in the signal region. The distribution labeled Up (Down) comes from varying the purity one sigma up (down). The systematic uncertainty resulting from this variation is around 5% at the low end of the p_T range and increases to 20% after $p_T > 400$ GeV.

2.6 Irreducible backgrounds

2.6.1 Simulation of V+γ Processes

The $Z(\rightarrow \nu\bar{\nu})+\gamma$ and $W(\rightarrow \ell\nu)+\gamma$ background contributions are modeled using MC simulations. Samples generated at the leading order (LO) in QCD by MADGRAPH 5 with up to two additional partons and a generator-level requirement of $E_T^\gamma > 130$ GeV are employed for this purpose.

A study using an aMC@NLO sample with high E_T^γ threshold confirms that the predicted kinematic distributions would not change drastically by using the NLO sample. Figures 2-16 and 2-17 show the comparisons of the aMC@NLO samples¹ and the MADGRAPH 5 samples used for the background estimation in the key kinematic distributions.

To approximate the QCD higher-order effects, $Z(\rightarrow \nu\bar{\nu})+\gamma$ and $W(\rightarrow \ell\nu)+\gamma$ events are reweighted with E_T^γ by the factors given in Tab. 2.6. These factors are the ratios of QCD next-to-next-to leading order (NNLO) differential cross sections

¹These samples were privately produced.

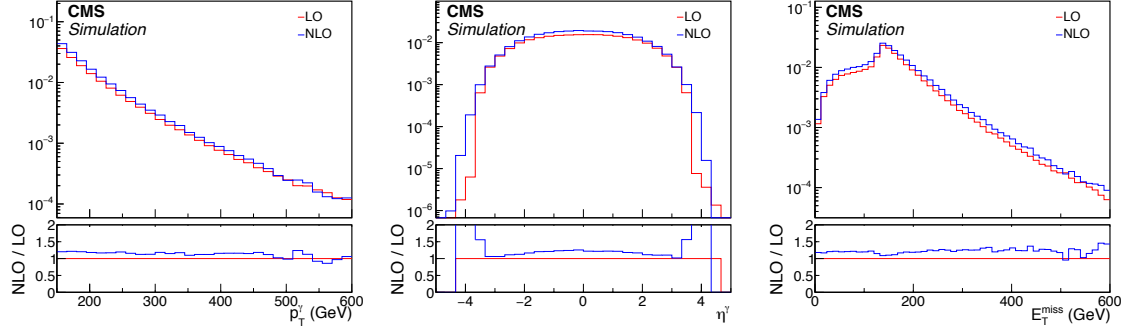


Figure 2-16: Distributions of E_T^γ (left), η^γ (middle), and p_T^Z (right) in $Z(\rightarrow \nu\bar{\nu}) + \gamma$ process from the private aMC@NLO sample (blue) and the LO sample used for background prediction (red) along with the NLO / LO ratios.

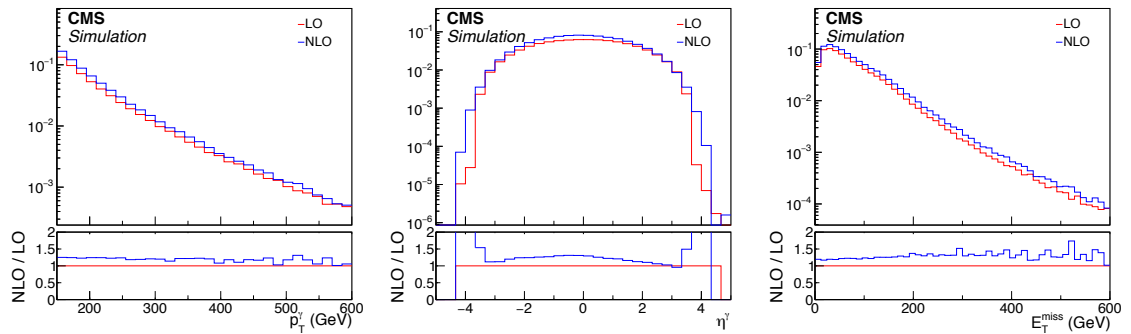


Figure 2-17: Distributions of E_T^γ (top left), η^γ (top right), and p_T^W (bottom left) in $W(\rightarrow \ell\nu) + \gamma$ process from the private aMC@NLO sample (blue) and the LO sample used for background prediction (red) along with the NLO / LO ratios.

E_T^γ range (GeV)	$Z(\rightarrow \nu\bar{\nu}) + \gamma$	$W(\rightarrow \ell\nu) + \gamma$
[175, 190]	1.44	1.40
[190, 250]	1.41	1.37
[250, 400]	1.35	1.31
[400, 700]	1.29	1.26
[700, ∞)	1.15	1.15

Table 2.6: Correction factors $k_{\text{QCD}}^{\text{NNLO}}$ for $Z(\rightarrow \nu\bar{\nu}) + \gamma$ and $W(\rightarrow \ell\nu) + \gamma$ samples.

calculated by Grazzini et al. [?] to the LO cross sections given in the centrally produced samples. Note that the denominator cross section includes contributions from processes with up to two additional partons, and is therefore not a LO cross section in the strict sense of the word. $V\gamma$ k-factors found in literature are $\gg 1$ at high E_T^γ , if the denominator only accounts for the cross section of $q\bar{q} \rightarrow V\gamma$ process.

Higher-order electroweak correction factors are also applied as a function of E_T^γ . Out of various electroweak higher-order effects, ones that can give sizeable ($\gg \mathcal{O}(\alpha)$) corrections to the cross section are the Sudakov suppression at high boson p_T and potentially the addition of photon-induced scattering processes [?, ?]. We apply the correction factors shown in Figure 2-18, which are the combinations of Sudakov suppression factors and photon-induced enhancements, and are provided by the authors of Ref. [?] in addition to the NNLO QCD correction.

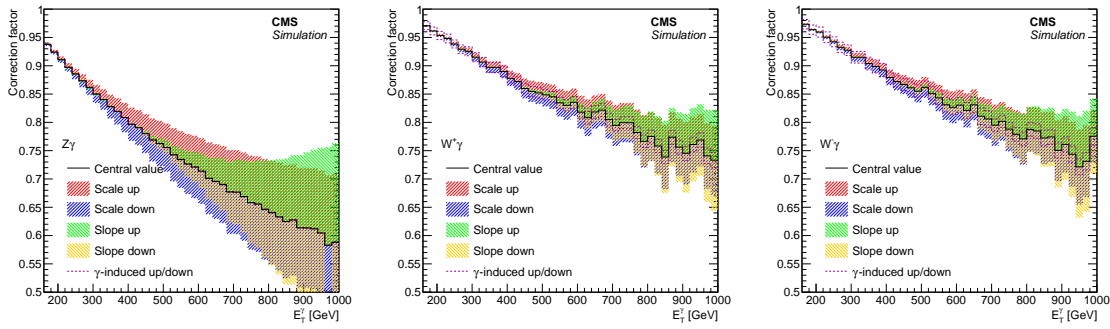


Figure 2-18: Electroweak NLO cross section corrections as a function of photon p_T for $Z(\rightarrow \nu\bar{\nu}) + \gamma$ (left), $W^+ + \gamma$ (middle), and $W^- + \gamma$ (right) processes, overlaid with uncertainty bands. See text for descriptions of the individual components of the uncertainty. The uncertainty due to γ -induced production is negligible in $Z(\rightarrow \nu\bar{\nu}) + \gamma$ production.

The differential cross section after the full higher-order corrections is

$$d\sigma_{\text{QCD}}^{\text{LO}} \cdot k_{\text{QCD}}^{\text{NNLO}} \cdot (1 + k_{\text{EW}}^{\text{Sudakov}} + k_{\text{EW}}^{q\gamma}) , \quad (2.6)$$

where $k_{\text{QCD}}^{\text{NNLO}} = d\sigma_{\text{QCD}}^{\text{NNLO}}/d\sigma_{\text{QCD}}^{\text{LO}}$, and the two k_{EW} terms are the Sudakov suppression and photon-induced enhancement components of the electroweak correction, respectively.

Furthermore, subtle differences between simulation and observation in the reconstruction and identification efficiencies for various particle candidates are accounted for with the set of selection efficiency correction factors ρ . The value of an individual ρ typically lies within a few percent of unity.

Four sources of systematic uncertainties considered for E_{T}^{γ} distribution ratios of the $V+\gamma$ processes are higher-order QCD corrections, higher-order EWK corrections, choice of PDF set, and data-to-simulation correction factors ρ . The four uncertainties are evaluated for each E_{T}^{γ} bin and fully correlated between the different bins..

The higher-order QCD renormalization and factorization scale uncertainties on the NNLO cross sections are assessed by varying the respective scales by factors 2 and 0.5 during the cross section computation. The uncertainties vary between 7-8% across the bins and are considered uncorrelated in the ratio between the $Z(\rightarrow \nu\bar{\nu})+\gamma$ and $W(\rightarrow \ell\nu)+\gamma$ processes.

Theoretical uncertainties on the electroweak corrections are not well understood to date. We estimate the magnitude of the uncertainty on $k_{\text{EW}}^{\text{Sudakov}}$ and $k_{\text{EW}}^{q\gamma}$ to be $(k_{\text{EW}}^{\text{Sudakov}})^2$ and $k_{\text{EW}}^{q\gamma}$, i.e., square of the correction for Sudakov suppression and the 100% of the correction itself for the photon-induced enhancement. The choice of using the square of $k_{\text{EW}}^{\text{Sudakov}}$ is motivated by the fact that fully resummed leading-log Sudakov suppression is an exponential of $k_{\text{EW}}^{\text{Sudakov}}$. This prescription is motivated by discussions with J. Lindert based on the paper [].

For the Sudakov suppression, which is the dominant term in the electroweak correction, we further consider two types of systematic variations, inspired by ref. [?], which provides a prescription for electroweak correction uncertainties for $V + \text{jets}$

processes. In this paper, electroweak correction as a function of the boson p_T is varied in overall scale and in slope. The slope variation is realized by selecting a point in the boson p_T spectrum and letting the shift in correction cross over at the point (see Figure 2-19). Following this prescription, we let the Sudakov suppression vary in overall scale and in slope, where we choose our crossover point for the slope variation to be at $E_T^\gamma = 590 \text{ GeV}$.

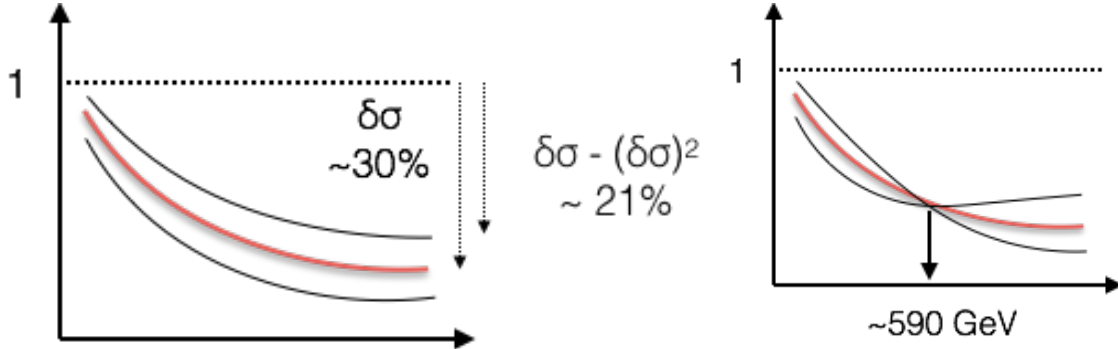


Figure 2-19: Electroweak correction variation scheme to cover the scale (left) and shape (right) uncertainties.

The PDF uncertainty is evaluated by varying the weight of each event using the weights provided in the NNPDF set, and taking the standard deviation of the resulting E_T^γ distributions. This uncertainty is considered fully correlated in the ratio between the $Z(\rightarrow \nu\bar{\nu})+\gamma$ and $W(\rightarrow \ell\nu)+\gamma$ processes, i.e., the variation of the ratio is bounded by the ratios formed by the simultaneous upward and downward variations of the numerator and denominator. .

Finally, data-to-simulation correction factors ρ for the lepton identification efficiencies have associated uncertainties that do not cancel when taking ratios between regions defined by different lepton selection requirements. The lepton efficiencies are measured using the “tag-and-probe” method where the tag object is an electron (muon) object passing the tight ID and matched to a SingleElectron (SingleMuon) trigger and the probe object is a PF electron (muon) without any ID applied. The passing (failing) categories are defined by events with probes passing (failing) the ID definition in question. The electron (muon) scale factors ρ are approximately unity with a flat 2% (1%) systematic uncertainty.

2.6.2 Data-driven Control Regions

Contributions from the $Z(\rightarrow \nu\bar{\nu})+\gamma$ and $W(\rightarrow \ell\nu)+\gamma$ processes are estimated using observed data in four mutually exclusive single-electron, single-muon, dielectron, and dimuon control regions. The various ratios between the expected $Z(\rightarrow \nu\bar{\nu})+\gamma$ yield in the combined signal regions and the expected $W(\rightarrow \ell\nu)+\gamma$ and $Z(\rightarrow \ell\bar{\ell})+\gamma$ yields in the control region are constrained by MC simulations. When a ratio is calculated using MC samples as a function of E_T^γ , it is referred to as the “transfer factor” between the two processes. This background estimation method exploits the cancellation of some of the systematic uncertainties, both experimental and theoretical, in the transfer factors between the different $V+\gamma$ processes.

For the transfer factor $R_{\ell\ell\gamma}^{Z\gamma}$, the numerator is the expected $Z(\rightarrow \nu\bar{\nu})+\gamma$ yield in the combined signal regions and the denominator is the expected $Z(\rightarrow \ell\bar{\ell})+\gamma$ yield in the relevant dilepton control region. The uncertainties due to photon energy calibration, jet energy resolution, and higher-order QCD effects are significantly reduced on $R_{\ell\ell\gamma}^{Z\gamma}$ compared to when such effects are considered for individual processes. The only uncertainties in the transfer factor $R_{\ell\ell\gamma}^{Z\gamma}$ that do not largely cancel are those on lepton identification efficiency, the statistical uncertainty due to the limited MC sample size, and a minor uncertainty due to the different acceptances between the $Z(\rightarrow \nu\bar{\nu})+\gamma$ and $Z(\rightarrow \ell\bar{\ell})+\gamma$ processes. Figure 2-20 shows the transfer factor $R_{ee\gamma}^{Z\gamma}$ ($R_{\mu\mu\gamma}^{Z\gamma}$) between the dielectron (dimuon) control region and the combined signal regions.

For increasing E_T^γ , the Z boson in a $Z(\rightarrow \ell\bar{\ell})+\gamma$ event tends to emerge with lower rapidity, and hence so do its decay products. As a consequence, the charged leptons are more likely to fall within the inner tracker acceptance, which increases the dilepton control region selection efficiency of these events. In contrast, the signal region selection efficiency of $Z(\rightarrow \nu\bar{\nu})+\gamma$ events is unaffected by the rapidity of the final state neutrinos, as long as the observed E_T^{miss} has the appropriate magnitude and azimuthal direction. This causes the distinctive drop in the ratio $R_{\ell\ell\gamma}^{Z\gamma}$ with increasing E_T^γ .

Using the transfer factor $R_{\ell\ell\gamma}^{Z\gamma}$, the total estimated event yield $T_{\ell\ell\gamma}$ in each dilepton

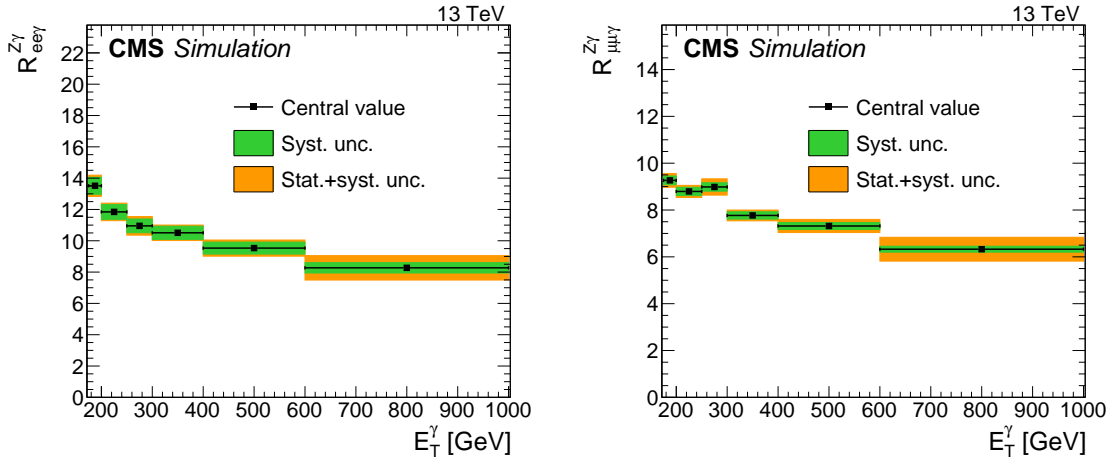


Figure 2-20: Transfer factors $R_{ee\gamma}^{Z\gamma}$ (left) and $R_{\mu\mu\gamma}^{Z\gamma}$ (right). The numerator is the expected $Z(\rightarrow \nu\bar{\nu})+\gamma$ yield in the combined signal regions and the denominator is the expected $Z(\rightarrow \ell\bar{\ell})+\gamma$ yield in the dielectron (left) or dimuon (right) control region. The uncertainty bands in green (inner) and orange (outer) show the systematic uncertainty, and the combination of systematic and statistical uncertainty arising from limited MC sample size, respectively. The systematic uncertainties considered are the uncertainties in the data-to-simulation correction factors ρ for the lepton identification efficiencies.

control region in the i^{th} bin of the E_T^γ distribution is given by

$$T_{\ell\ell\gamma,i} = \frac{N_i^{Z\gamma}}{R_{\ell\ell\gamma,i}^{Z\gamma}} + b_{\ell\ell\gamma,i}, \quad (2.7)$$

where $N^{Z\gamma}$ is the predicted number of $Z(\rightarrow \nu\bar{\nu})+\gamma$ events in the combined signal regions and $b_{\ell\ell\gamma}$ is the predicted contribution from other background sources in the dilepton control region, namely $t\bar{t}\gamma$, $VV\gamma$, and misidentified hadrons. The subscript i indicates that the quantities are evaluated in bin i of the E_T^γ distribution.

Similar considerations apply to events arising from the $W(\rightarrow \ell\nu)+\gamma$ process. A large fraction of such events are rejected by the electron and muon vetoes in the signal region selection and end up in the control regions instead. However, hadronic tau events and events where the leptons are out of acceptance or fail to be reconstructed will remain in the signal region, on top of the vetoes having imperfect efficiencies. In the ratio of these two classes of events, denoted $R_{\ell\gamma}^{W\gamma}$, the only uncertainties that remain non-negligible are those associated with the lepton identification efficiency

Subprocess	$A \times \epsilon \times 10^3$
$W \rightarrow e\nu + \gamma$	1.68
	$ \eta^e < 2.5$
	$ \eta^e > 2.5$
$W \rightarrow \mu\nu + \gamma$	1.83
	$ \eta^\mu < 2.5$
	$ \eta^\mu > 2.5$
$W \rightarrow \tau\nu + \gamma$	5.03

Table 2.7: The breakdown of simulated $W + \gamma$ events passing the full event selection. Events are categorized in the W decay mode. Events with $e\nu$ and $\mu\nu$ final states are further divided into those where the lepton is roughly within acceptance ($|\eta| < 2.5$) but failed the lepton veto, and those where the lepton is out of acceptance ($|\eta| > 2.5$). For each W decay mode, the fraction out of total generated ($A \times \epsilon$) is shown.

and the MC statistical uncertainty.

Table 2.7 gives the breakdown of the $W(\rightarrow \ell\nu) + \gamma$ background passing the full event selection for the signal region, categorized by the lepton flavor and, for the case of electrons and muons, the lepton pseudorapidity at the parton-level. From this breakdown, one sees that events where the W boson decays to a τ and a neutrino constitute approximately 60% of the $W(\rightarrow \ell\nu) + \gamma$ background. The remaining 40% of the $W(\rightarrow \ell\nu) + \gamma$ background comes from events where the W boson decays to a μ or e and a neutrino. Events containing an electron are more likely to be within the detector acceptance, while those with a muon are more likely to be out of acceptance. For the in-acceptance background ($|\eta| < 2.5$), the identification efficiency, which is lower for electrons than for muons, which translates to a larger background contribution from the electrons. The requirement for large E_T^{miss} removes events with out-of-acceptance electrons because the energy from these electrons is captured by the calorimeters and retains events with out-of-acceptance muons because they contribute directly to the missing momentum. The overall result is a larger background contribution from events with out-of-acceptance muons than from events with out-of-acceptance electrons.

Figure 2-21 shows the transfer factor $R_{e\gamma}^{W\gamma}$ ($R_{\mu\gamma}^{W\gamma}$) between the single-electron (single-muon) control region and the combined signal regions, for which the numer-

ator is the estimated $W(\rightarrow \ell\nu)+\gamma$ yield in the combined signal regions, and the denominator is the estimated $W(\rightarrow \ell\nu)+\gamma$ yield in the relevant control region. The ratio $R_{e\gamma}^{W\gamma}$ decreases with increasing E_T^γ in a similar manner to $R_{\ell\ell\gamma}^{Z\gamma}$. The underlying logic is the same; e.g., that the signal region selection efficiency is unaffected by E_T^γ while the control region acceptances increase with increasing E_T^γ due to increased lepton efficiency resulting from lower W rapidity.

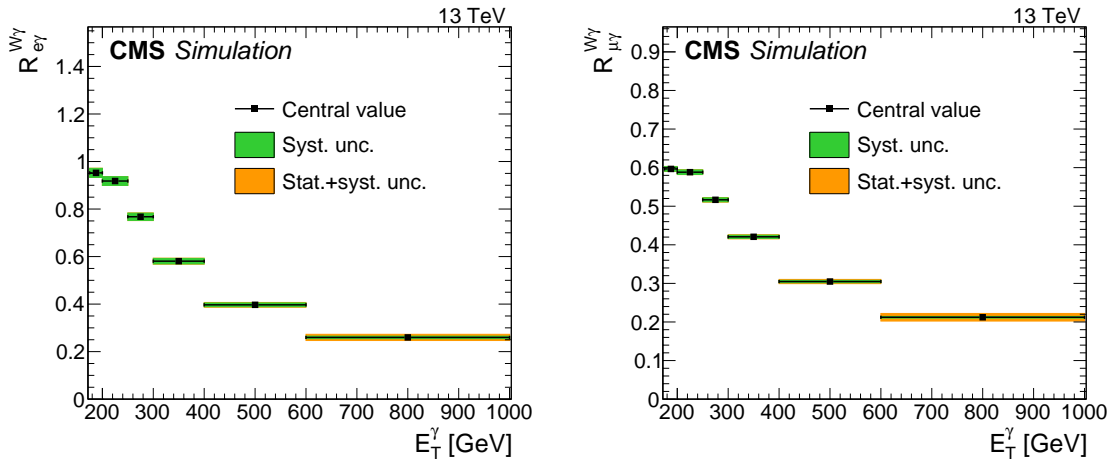


Figure 2-21: Transfer factors $R_{e\gamma}^{W\gamma}$ (left) and $R_{\mu\gamma}^{W\gamma}$ (right). The numerator is the expected $Z(\rightarrow \nu\bar{\nu})+\gamma$ yield in the combined signal regions and the denominator is the expected $W(\rightarrow \ell\nu)+\gamma$ yield in the mono-electron (left) or mono-muon (right) control region. The uncertainty bands in green (inner) and orange (outer) show the systematic uncertainty, and the combination of systematic and statistical uncertainty arising from limited MC sample size, respectively. The systematic uncertainties considered are the uncertainties in the data-to-simulation correction factors ρ for the lepton identification efficiencies.

Finally, to benefit further from the larger statistical power that the single-lepton control samples provides, an additional transfer factor $f_{W\gamma}^{Z\gamma} = N^{Z\gamma}/N^{W\gamma}$ is defined to connect the $Z(\rightarrow \nu\bar{\nu})+\gamma$ and $W(\rightarrow \ell\nu)+\gamma$ background yields in the signal regions, where the quantity $N^{W\gamma}$ is the number of $W(\rightarrow \ell\nu)+\gamma$ events in the combined signal regions. When calculating the ratio $f_{W\gamma}^{Z\gamma}$, all experimental uncertainties associated with the data-to-simulation correction factors ρ cancel since both processes result in very similar event configurations. The main uncertainties in $f_{W\gamma}^{Z\gamma}$ are those from higher-order theoretical corrections, discussed in Section 2.6.1. Figure 2-22 shows the effect of each systematic uncertainty in $f_{W\gamma}^{Z\gamma}$ with respects to its nominal value for

$Z(\rightarrow \nu\bar{\nu})+\gamma$ and $W(\rightarrow \ell\nu)+\gamma$, respectively.

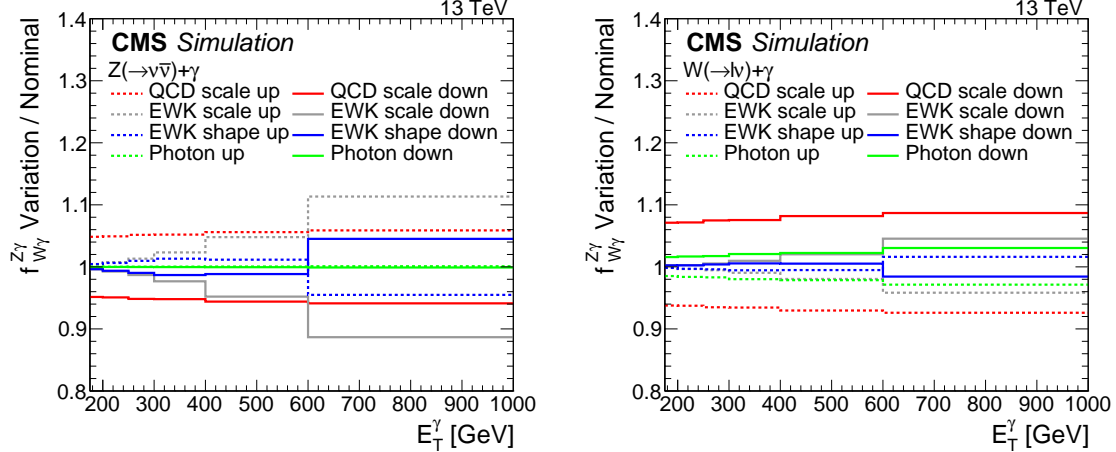


Figure 2-22: Systematic uncertainty in the transfer factors for $Z(\rightarrow \nu\bar{\nu})+\gamma$ (left) and $W(\rightarrow \ell\nu)+\gamma$ (right). The last bin includes all events with $E_T^\gamma > 1000$ GeV.

The ratio $f_{W\gamma}^{Z\gamma}$ rises rather than falls with increasing E_T^γ because $W(\rightarrow \ell\nu)+\gamma$ events have a lower signal region selection efficiency when the charged lepton falls within the tracker acceptance due to the lepton veto while the $Z(\rightarrow \nu\bar{\nu})+\gamma$ efficiency is independent of E_T^γ . Figure 2-23 shows the transfer factor $f_{W\gamma}^{Z\gamma}$ between the $Z(\rightarrow \nu\bar{\nu})+\gamma$ and $W(\rightarrow \ell\nu)+\gamma$ processes in the combined signal region.

Using $R_{\ell\gamma}^{W\gamma}$ and $f_{W\gamma}^{Z\gamma}$, the total estimated event yield $T_{\ell\gamma}$ in each single-lepton control region in the i^{th} bin of the E_T^γ distribution is given by

$$T_{\ell\gamma,i} = \frac{N_i^{Z\gamma}}{R_{\ell\gamma,i}^{W\gamma} f_{W\gamma,i}^{Z\gamma}} + b_{\ell\gamma,i}, \quad (2.8)$$

where $b_{\ell\gamma}$ is the predicted contribution from other background sources in the single-lepton regions, namely misidentified electrons and hadrons and other minor SM processes.

2.7 Beam halo

Bremsstrahlung photons emitted by beam halo muons in the ECAL volume generate a physical EM shower in the ECAL crystals. Large deposits energy are rare, but the

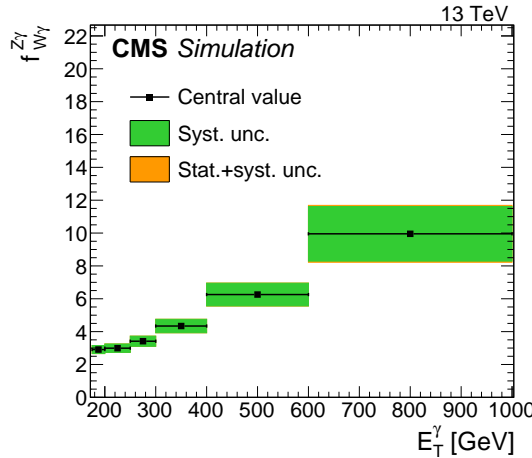


Figure 2-23: Transfer factor $f_{W\gamma}^{Z\gamma}$ in the combined signal regions. The numerator is the expected $Z(\rightarrow \nu\bar{\nu})+\gamma$ yield and the denominator is the expected $W(\rightarrow \ell\nu)+\gamma$ yield. The uncertainty bands in green (inner) and orange (outer) show the systematic uncertainty, and the combination of systematic and statistical uncertainty arising from limited MC sample size, respectively. The systematic uncertainties considered are the uncertainties from higher-order theoretical corrections.

rate of beam halo penetration during the 2016 run was substantial. The characteristic features of a shower caused by a halo particle include coincident hits in the barrel muon system and a “trail” of low-energy clusters in ECAL along the particle trajectory. The beam halo MET filter described in Section 1.2.6 exploits the former, while the E_{MIP} variable described in Section 1.2.3 captures the latter.

Because beam halo particles are produced through complex LHC machine effects, the observed distribution of the halo showers is not symmetric in the azimuthal angle in the detector coordinates. The right side of Figure 2-24 is a ϕ^γ distribution of the halo showers obtained from the SinglePhoton dataset, requiring $E_{\text{T}}^{\text{miss}} > 140$ GeV. Halo showers are defined as those that fail the MIP-tagging and in the event tagged by the CSC beam halo tagger. On the other hand, reconstructed showers from all other sources are symmetric in ϕ^γ as shown on the left side of Figure 2-24.

For the distribution of Fig. 2-24 to be a valid template for halo showers, it must be first confirmed that its shape is invariant under photon selection requirements. However, further study of the ϕ^γ distribution of the halo showers indicates that the relative strength of the two prominent peaks in the distribution may change under

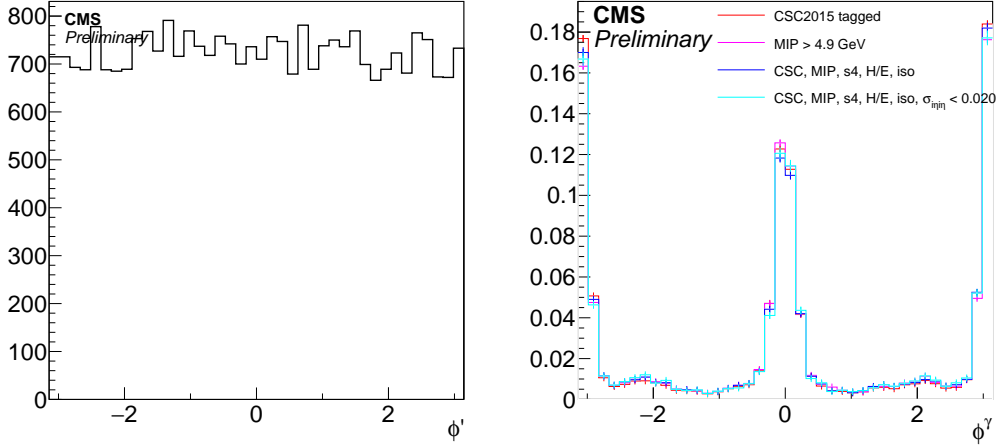


Figure 2-24: Left: The ϕ^γ distribution from $Z(\rightarrow \nu\bar{\nu})+\gamma$ MC simulation. Right: The ϕ^γ distribution of the halo-like showers, tagged in multiple ways. Histograms are normalized to unity. The cyan histogram is the ϕ^γ distribution after applying photon identification selections except for the shower shape. It can be seen that the ϕ^γ distribution is highly stable against the listed identification selections.

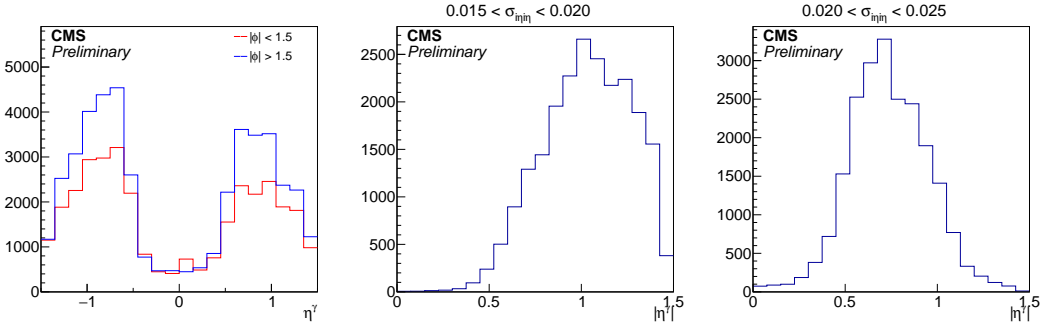


Figure 2-25: Left: η distribution of the halo-like showers with $|\phi| < \pi/2$ and $|\phi| > \pi/2$. Middle and right: shift in the η distribution of the halo-like showers with respect to the requirement on σ_{inj} .

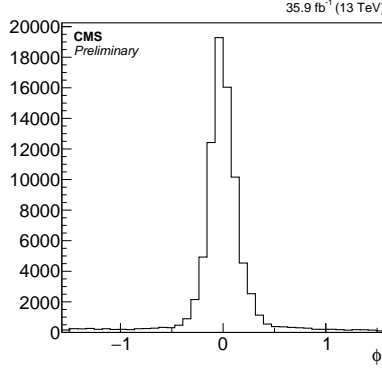


Figure 2-26: Folded ϕ' distribution of the halo sample.

the $\sigma_{i\eta i\eta}$ selection requirement. To explain this phenomenon, one needs to look at the the η^γ distribution of the shower populations near $\phi^\gamma \sim 0$ and $\phi^\gamma \sim \pi$, shown in the top portion of Figure 2-25. Meanwhile, halo showers tend to have narrower shape in the η direction when occurring at high η , due to the projective geometry of the ECAL crystals, visible in the bottom portion of Figure 2-25 bottom). Combining the two observations, the conclusion is that the stringent requirement on the narrowness of the shower in the photon selection will preferentially reduce the $\phi \sim 0$ population.

Nevertheless, the invariance under photon selection is recovered by folding the ϕ^γ distribution such that the two peaks of the halo showers coincide. To match the positions of the peaks in the halo template, the distribution is shifted by 0.005 and then folded along 0. The new angular variable ϕ'

$$\phi' := \left| \left[[\phi^\gamma + 0.005]_{-\pi}^{\pi} - \frac{\pi}{2} \right]_{-\pi}^{\pi} \right| - \frac{\pi}{2}, \quad (2.9)$$

where $[\cdot]_\pi^\pi$ signifies casting the content into range $[-\pi, \pi]$, exhibits a unimodal distribution for the halo template, as shown in Fig. 2-26.

The contribution of real photons into the halo control sample is negligible. This is confirmed from the $\sigma_{i\eta i\eta}$ distribution of the halo control sample and the correlation between $\sigma_{i\eta i\eta}$ and E_{MIP} in a MC true-photon sample. The $\sigma_{i\eta i\eta}$ distribution of the halo control sample features a small peak at $\sigma_{i\eta i\eta} \sim 0.01$, which can be attributed to contributions from true photons, as the photon $\sigma_{i\eta i\eta}$ distribution overlaid in Fig-

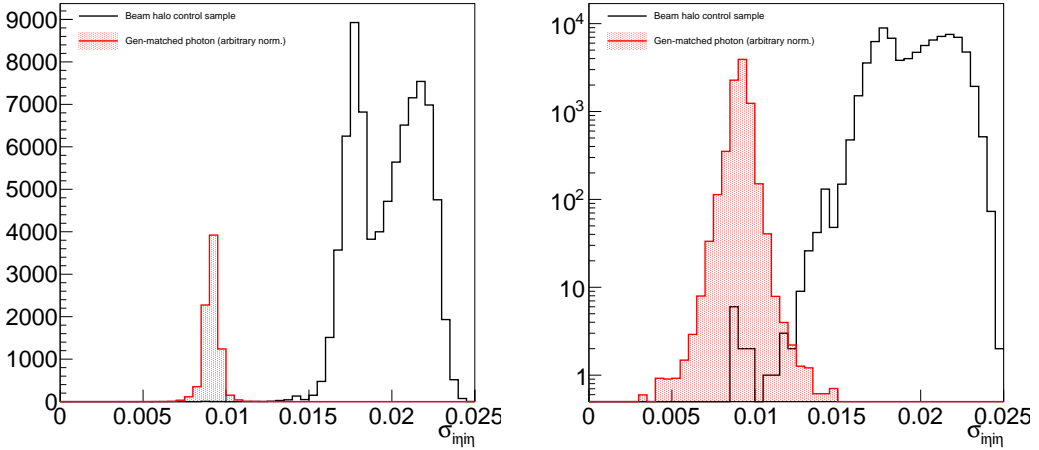


Figure 2-27: The $\sigma_{i\eta i\eta}$ distribution of the beam halo control sample and a reference distribution from truth-matched MC photons. Left: linear scale, Right: log scale. There is a small peak at $\sigma_{i\eta i\eta} \sim 0.01$ in the beam halo control sample, which is not visible in linear-scale.

ure 2-27 suggests. However, the contribution of true photons diminishes rapidly with increasing $\sigma_{i\eta i\eta}$. Additionally, Figure 2-28 illustrates that the shape of the true-photon $\sigma_{i\eta i\eta}$ does not change significantly with respect to E_{MIP} . From these two observations, we can see that there are only a negligible number of true photons in the halo control sample.

While the peaking behavior is a robust feature of the halo showers, their rate is not easily predictable. Therefore, a two-template fit to the ϕ' distribution of the photons in the candidate sample, where the templates are a uniform distribution (Figure 2-24 left) and that of the halo shower (Figure 2-26), accurately estimates the amount of beam halo background present in the signal region. For this analysis, the splitting of the signal region functions in a similar manner, enabling us to determine the beam halo contribution during the signal extraction procedure.

In the horizontal (H) and vertical (V) signal regions, collision processes occupy the relative fractions of phase space $C_H = 1/\pi$ and $C_V = (\pi - 1)/\pi$ corresponding to $|\phi'| < 0.5$ and $0.5 < |\phi'| < \pi/2$, respectively. The corresponding fractions for beam halo events are determined by selecting a halo-enriched sample where the halo veto is inverted. Thus, a fit of the two signal regions provides an estimate of the overall

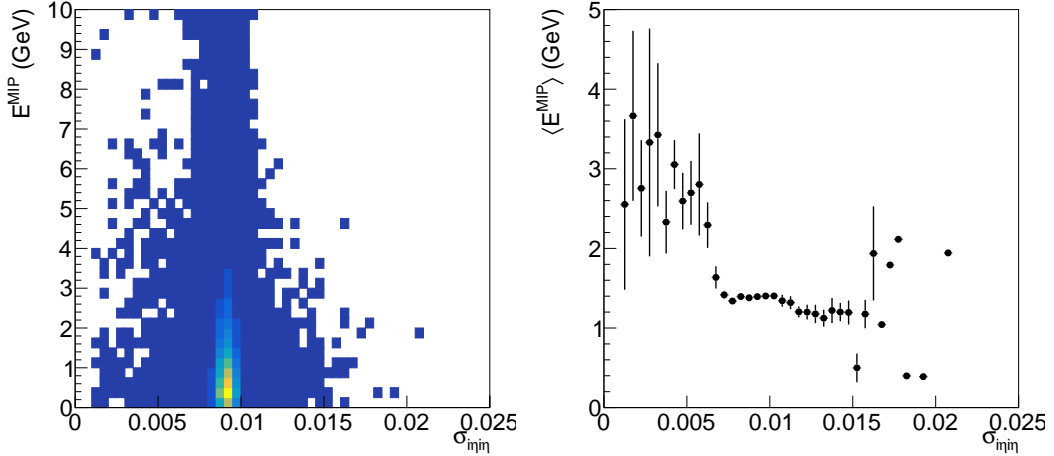


Figure 2-28: Correlation between $\sigma_{i\eta i\eta}$ and E_{MIP} in truth-matched MC photons. Left: $E_{\text{MIP}}-\sigma_{i\eta i\eta}$ distribution. Right: average E_{MIP} in bins of $\sigma_{i\eta i\eta}$.

normalization of the beam halo background, denoted h .

The E_{T}^{γ} dependence of the halo background is encoded in $n_{K,i}^{\text{halo}}$, the unit-normalized beam halo prediction in the i^{th} bin of the signal region $K \in \{H, V\}$. Using the notation introduced in Section 2.6, the total estimated background T_K in the two signal regions are

$$\begin{aligned} T_{K,i} &= C_K \left[N_i^{Z\gamma} + N_i^{W\gamma} + b_{K,i} \right] + h n_{K,i}^{\text{halo}} \\ &= C_K \left[(1 + f_{W\gamma i}^{Z\gamma -1}) N_i^{Z\gamma} + b_{K,i} \right] + h n_{K,i}^{\text{halo}}, \end{aligned} \quad (2.10)$$

where $b_{K,i}$ is the total contribution to bin i of region K from electron and hadron misidentification, ECAL spikes, and other minor SM background processes.

2.8 Spikes

Given the observations in Section 1.3.2, the time distribution of spike-like rec hits outside of the window $-15 < t < -10$ ns (and the equivalent with one-bunch-crossing shift) is understood to be due to delayed interactions of neutral hadrons with the APDs, as documented also in Ref. [?]. In other words, ECAL spike clusters which

survive the time cleaning cut of the standard reconstruction are a part of a broad tail of a distribution, and there is no evidence of spike signals that specifically populate the “in-time” region $-3 < t < 3$ ns.

Having established that there is no special population of ECAL spikes in the in-time region, we can estimate the number of ECAL spike events present in the signal candidate sample by an “ABCD” method, where

- A = Number of clusters with $\sigma_{i\eta i\eta}$ or $\sigma_{i\phi i\phi}$ less than 0.001 and seed time $-15 < t < -10$ ns, counted in the special-reconstruction sample,
- B = Number of clusters with both $\sigma_{i\eta i\eta}$ and $\sigma_{i\phi i\phi}$ greater than 0.001 and seed time $-15 < t < -10$ ns, counted in the special-reconstruction sample,
- C = Number of clusters with $\sigma_{i\eta i\eta}$ or $\sigma_{i\phi i\phi}$ less than 0.001 but an in-time seed, counted in the standard-reconstruction sample passing all other signal event selection,

and D is the estimated number of spike events in the signal region, obtained by

$$D = C \times \frac{B}{A}. \quad (2.11)$$

The special-reconstruction samples for A and B are from the SinglePhoton datasets, with only the timing cleaning removed from the offline reconstruction. In this way, the selection bias over spikes from the L1T, HLT, and offline reconstruction is equally applied to samples A, B, and C.

Plugging in the observed numbers, we have

$$A = 4969$$

$$B = 1180$$

$$C = 54$$

$$\therefore D = 12.8 \pm 1.8(\text{stat.})$$

There are, however, at least two reasons to believe that this method overestimates

the number of spike events in the signal region. One is that the population C contains some physical, prompt photon clusters that just happens to be narrow, as observed in Fig. 1-9. Another reason is that there is likely a correlation between the cluster width and the seed time such that the ratio of true D to C is smaller than B/A . This statement is based on the standard hypothesis that the wide-cluster spike is an ECAL spike embedded in a physical EM shower cluster. Under this model, spikes in wide clusters are mainly caused by prompt neutral hadrons in a jet, which implies that they strongly prefer seed time $-15 < t < -10$ ns. Given that this is a minor background with a relatively large uncertainty, as described below, we will still use this estimate as the nominal value of predicted spike contribution in the signal region.

The uncertainty in the estimate of D is evaluated by two modifications to A, B, and C. First, the three values are recomputed with using $\sigma_{i\eta i\eta} < 0.001$ as the only definition of narrow cluster. This results in a minor change of the value of D of 12.1 ± 1.7 . Next, A and B are computed using a lower- p_T SinglePhoton sample, requiring triggers Photon135_PFMET100 or Photon120_R9Id90_HE10_IsoM to have fired, instead of the signal trigger. The second modification gives $D = 9.1 \pm 1.3$. We then take twice the discrepancy between the nominal D and the D value from the second modification as the systematic uncertainty in the spike background estimate.

2.9 Minor SM Backgrounds

After the full selection described in Section 2.2, the SM $\gamma + \text{jets}$, $t\bar{t}\gamma$, $VV\gamma$, $Z(\rightarrow \ell\bar{\ell}) + \gamma$, and $W \rightarrow \ell\nu$ processes are minor ($\sim 10\%$) background processes in the signal region. These processes, collectively denoted as minor SM backgrounds, contribute in the signal region when the jet energy is severely mismeasured or the leptons fail to be reconstructed resulting in large E_T^{miss} in the signal region. However, the E_T^{miss} is typically aligned with the photon or one of the jets in such cases, and therefore various selections on the kinematic relations between the E_T^{miss} , photons, and jets are used to reduce these backgrounds to a manageable rate. The estimates for all five processes are taken from MADGRAPH5_aMC@NLO [1] simulations at LO in QCD and

are listed in Tables 2.8 and 2.9.

2.10 Statistical Interpretation

The potential signal contribution is extracted from the data via simultaneous fits to the E_T^γ distributions in the signal and control regions defined in Section 2.2. Uncertainties in various quantities are represented by nuisance parameters in the fit. Predictions for $Z(\rightarrow \nu\bar{\nu})+\gamma$, $W(\rightarrow \ell\nu)+\gamma$, and the beam halo backgrounds are varied in the fit. Beam halo is not a major background, but the extraction of its rate requires a fit to the observed distributions in the signal region.

Free parameters of the fit are the yield of $Z(\rightarrow \nu\bar{\nu})+\gamma$ background in each bin of the signal regions ($N_i^{Z\gamma}$) and the overall normalization of the beam halo background (h). Bin-by-bin yields of $W(\rightarrow \ell\nu)+\gamma$ and $Z(\rightarrow \ell\bar{\ell})+\gamma$ samples in all regions are related to the yield of $Z(\rightarrow \nu\bar{\nu})+\gamma$ through the MC prediction through the transfer factors defined in Section 2.6. The transfer factors are allowed to shift within the aforementioned theoretical and experimental uncertainties.

The background-only likelihood that is maximized in the fit is

$$\begin{aligned} \mathcal{L} &= \prod_i \{ \mathcal{L}_{\text{signal}} \times \mathcal{L}_{\text{single-lepton}} \times \mathcal{L}_{\text{dilepton}} \} \times \mathcal{L}_{\text{nuisances}} \\ &= \prod_i \left\{ \prod_{K=H,V} \mathcal{P}(d_{K,i} \mid T_{K,i}(\vec{\theta})) \times \prod_{\ell=e,\mu} \mathcal{P}(d_{\ell\gamma,i} \mid T_{\ell\gamma,i}(\vec{\theta})) \times \prod_{\ell=e,\mu} \mathcal{P}(d_{\ell\ell\gamma,i} \mid T_{\ell\ell\gamma,i}(\vec{\theta})) \right\} \times \prod_j \mathcal{N}(\theta_j) \\ &= \prod_i \left\{ \begin{array}{l} \prod_{K=H,V} \mathcal{P}\left(d_{K,i} \mid \left(1 + f_{W\gamma,i}^{Z\gamma}(\vec{\theta})\right) C_K N_i^{Z\gamma} + h n_{K,i}^{\text{halo}}(\vec{\theta}) + C_K b_{K,i}(\vec{\theta})\right) \\ \times \prod_{\ell=e,\mu} \mathcal{P}\left(d_{\ell\gamma,i} \mid \frac{N_i^{Z\gamma}}{R_{\ell\gamma,i}^{W\gamma}(\vec{\theta}) f_{W\gamma,i}^{Z\gamma}(\vec{\theta})} + b_{\ell\gamma,i}(\vec{\theta})\right) \\ \times \prod_{\ell=e,\mu} \mathcal{P}\left(d_{\ell\ell\gamma,i} \mid \frac{N_i^{Z\gamma}}{R_{\ell\ell\gamma,i}^{Z\gamma}(\vec{\theta})} + b_{\ell\ell\gamma,i}(\vec{\theta})\right) \end{array} \right\} \times \prod_j \mathcal{N}(\theta_j), \end{aligned} \quad (2.12)$$

following the notation introduced in Section 2.6, and where $\mathcal{P}(n|\lambda)$ is the Poisson probability of n for mean λ , \mathcal{N} denotes the unit normal distribution, and $d_{X,i}$ is the observed number of events in bin i of region X . Systematic uncertainties are treated

as nuisance parameters in the fit and are represented by $\vec{\theta}$. Each quantity Q_j with a nominal value \bar{Q}_j and a standard deviation of the systematic uncertainty σ_j appears in the likelihood function as $\bar{Q}_j \exp(\sigma_j \theta_j)$.

2.11 Results

2.11.1 Pre-fit and post-fit distributions

Figure 2-29 shows the observed E_T^γ distributions in the four control regions compared with the results from simulations before and after performing the simultaneous fit across all the control samples and signal region, and assuming absence of any signal. Figure 2-30 shows the observed E_T^γ distributions in the horizontal and vertical signal regions compared with the results from simulations before and after performing a combined fit to the data in all the control samples and the signal region. The observed distributions are in agreement with the prediction from SM and noncollision backgrounds.

E_T^γ [GeV]	[175, 200]	[200, 250]	[250, 300]	[300, 400]	[400, 600]	[600, 1000]
$Z\gamma$	81.2 ± 8.0	88.2 ± 8.4	38.8 ± 4.8	26.8 ± 3.7	8.8 ± 1.9	1.4 ± 0.7
$W\gamma$	27.9 ± 3.7	29.9 ± 3.9	11.4 ± 1.7	6.3 ± 1.2	1.4 ± 0.4	0.1 ± 0.1
Misid. electrons	22.5 ± 2.7	25.7 ± 2.7	10.5 ± 1.0	8.2 ± 0.7	2.7 ± 0.2	0.5 ± 0.0
Misid. hadrons	5.2 ± 2.2	9.3 ± 1.8	3.1 ± 0.7	1.0 ± 0.3	0.4 ± 0.1	0.0 ± 0.0
Other SM	13.6 ± 2.0	19.6 ± 1.3	13.9 ± 0.4	4.2 ± 0.2	0.8 ± 0.0	0.1 ± 0.0
ECAL spikes	4.3 ± 1.3	2.7 ± 0.8	0.5 ± 0.1	0.1 ± 0.0	0.0 ± 0.0	0.0 ± 0.0
Total prediction	154.6 ± 8.3	175.4 ± 8.8	78.2 ± 5.3	46.6 ± 4.0	14.1 ± 2.1	2.1 ± 0.8
Observed	150 ± 12	166 ± 13	76.0 ± 8.7	44.0 ± 6.6	19.0 ± 4.4	4.0 ± 2.0

Table 2.8: Expected event yields in each E_T^γ bin for various background processes in the horizontal signal region. The background yields and the corresponding uncertainties are obtained after performing a combined fit to data in all the control samples, excluding data in the signal region. The observed event yields in the horizontal signal region are also reported.

The expected yields in each bin of E_T^γ for all backgrounds in the horizontal and vertical signal regions after performing a combined fit to data in all the control samples, excluding data in the signal regions, are given in Tables 2.8 and 2.9, respectively.

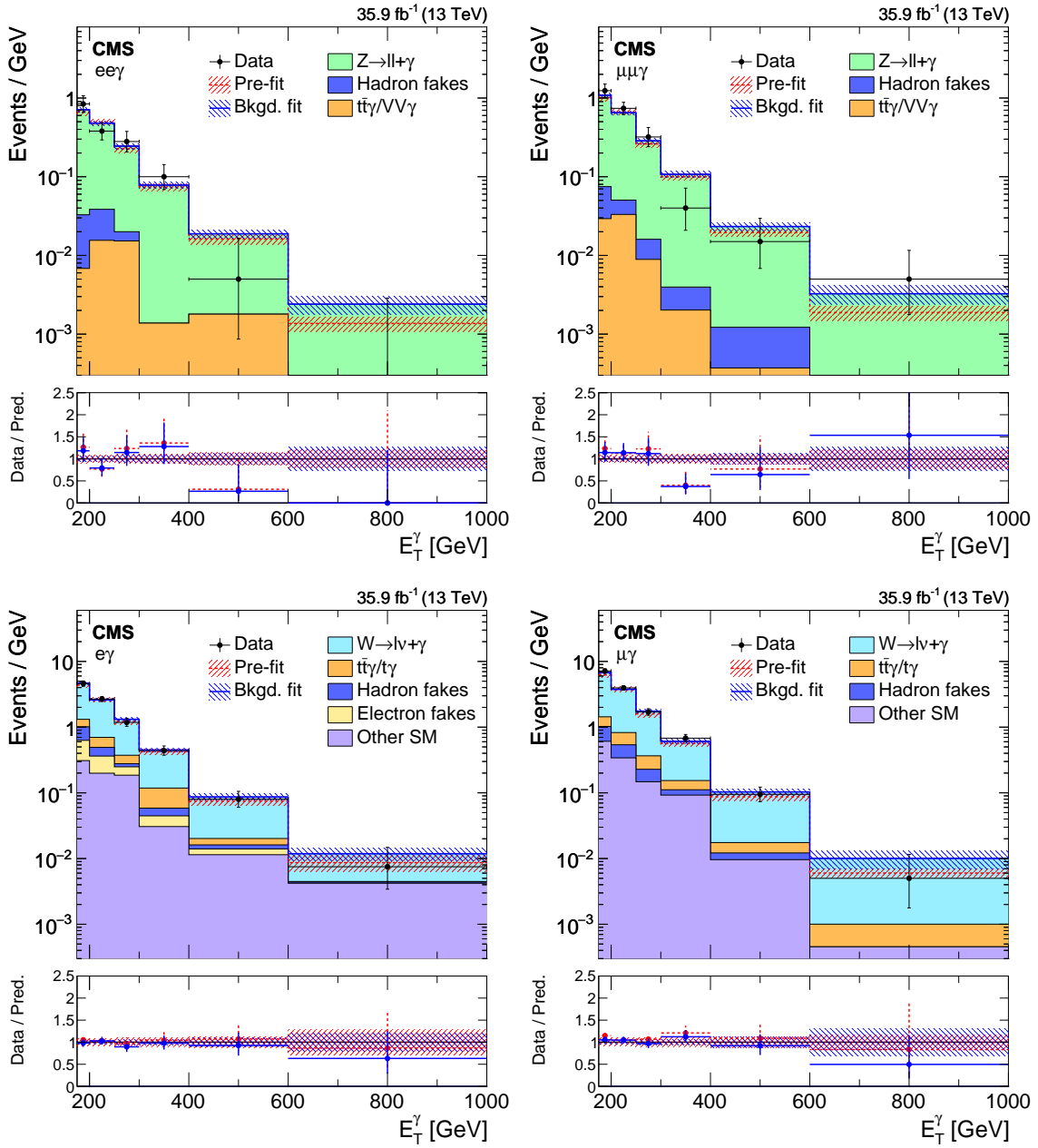


Figure 2-29: Comparison between data and MC simulation in the four control regions: $ee\gamma$ (upper left), $\mu\mu\gamma$ (upper right), $e\gamma$ (lower left), $\mu\gamma$ (lower right) before and after performing the simultaneous fit across all the control samples and signal region, and assuming absence of any signal. The last bin of the distribution includes all events with $E_T^\gamma > 1000$ GeV. The ratios of data with the pre-fit background prediction (red dashed) and post-fit background prediction (blue solid) are shown in the lower panels. The bands in the lower panels show the post-fit uncertainty after combining all the systematic uncertainties.

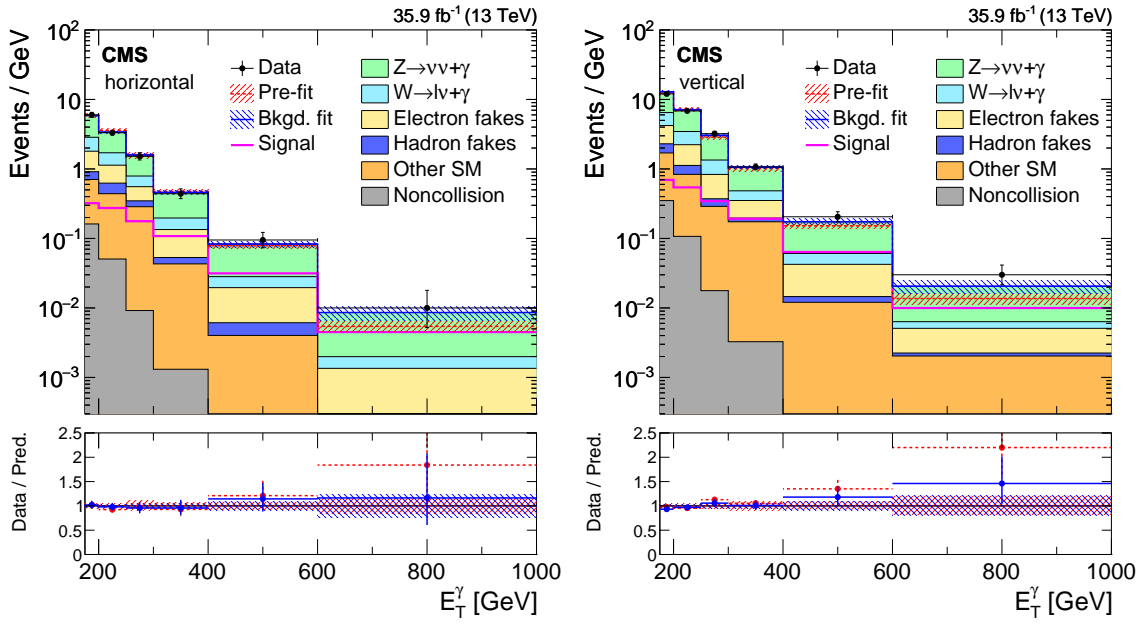


Figure 2-30: Observed E_T^γ distributions in the horizontal (left) and vertical (right) signal regions compared with the post-fit background expectations for various SM processes. The last bin of the distribution includes all events with $E_T^\gamma > 1000$ GeV. The expected background distributions are evaluated after performing a combined fit to the data in all the control samples and the signal region. The ratios of data with the pre-fit background prediction (red dashed) and post-fit background prediction (blue solid) are shown in the lower panels. The bands in the lower panels show the post-fit uncertainty after combining all the systematic uncertainties. The expected signal distribution from a 1 TeV vector mediator decaying to 1 GeV DM particles is overlaid.

E_T^γ [GeV]	[175, 200]	[200, 250]	[250, 300]	[300, 400]	[400, 600]	[600, 1000]
$Z\gamma$	172 ± 17	190 ± 18	83 ± 10	58.6 ± 7.9	18.0 ± 3.9	3.1 ± 1.6
$W\gamma$	59.9 ± 7.8	63.6 ± 7.8	24.6 ± 3.5	13.4 ± 2.4	3.0 ± 0.8	0.3 ± 0.2
Misid. electrons	48.4 ± 5.6	56.2 ± 5.1	23.4 ± 1.8	15.7 ± 1.4	5.6 ± 0.4	1.2 ± 0.1
Misid. hadrons	15.1 ± 4.4	14.5 ± 3.1	4.2 ± 0.8	2.3 ± 0.8	0.5 ± 0.1	0.1 ± 0.1
Other SM	33.8 ± 4.1	36.6 ± 2.7	13.6 ± 0.5	17.1 ± 0.6	2.4 ± 0.1	0.8 ± 0.0
ECAL spikes	9.3 ± 2.8	5.7 ± 1.7	0.9 ± 0.3	0.3 ± 0.1	0.0 ± 0.0	0.0 ± 0.0
Total prediction	339 ± 18	366 ± 19	150 ± 11	107.5 ± 8.7	29.6 ± 4.3	5.4 ± 1.7
Observed	301 ± 17	342 ± 19	161 ± 13	107 ± 10	41.0 ± 6.4	12.0 ± 3.5

Table 2.9: Expected event yields in each E_T^γ bin for various background processes in the vertical signal region. The background yields and the corresponding uncertainties are obtained after performing a combined fit to data in all the control samples, excluding data in the signal regions. The observed event yields in the vertical signal region are also reported.

The covariances between the predicted background yields across all the E_T^γ bins in the two signal regions are shown in Fig. 2-31. The expected yields together with the covariances can be used with the simplified likelihood approach detailed in Ref. [?] to reinterpret the results for models not studied in this thesis

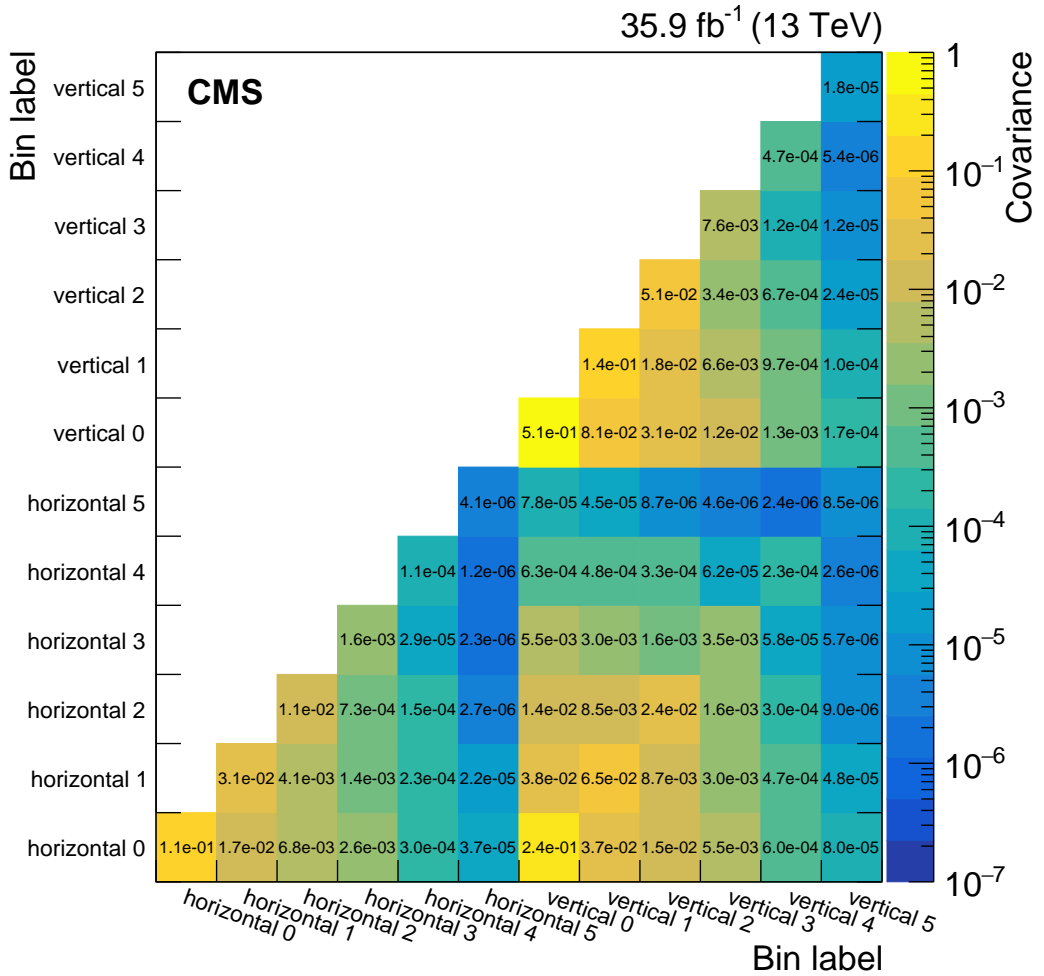


Figure 2-31: Covariances between the predicted background yields in all the E_T^γ bins of the horizontal and vertical signal regions. The bin labels specify which signal region the bin belongs to and what number bin it is for that region.

2.11.2 Limits

No significant excess of events beyond the SM expectation is observed. Upper limits are determined for the production cross section of the new-physics processes mentioned in Section ???. For each model, a 95% confidence level (CL) upper limit is obtained utilizing the asymptotic CL_s criterion [?, ?, ?], using a test statistic based on the negative logarithm of the likelihood in Section 2.10.

Figure 2-32 shows the 95% CL upper cross section limits with respect to the corresponding theoretical cross section ($\mu_{95} = \sigma_{95\%}/\sigma_{\text{theory}}$) for the vector and axial-vector mediator scenarios, in the $M_{\text{med}} - m_{\text{DM}}$ plane. The solid black (dashed red) curves are the observed (expected) contours of $\mu_{95} = 1$. The σ_{theory} hypothesis is excluded at 95% CL or above in the region with $\mu_{95} < 1$. The uncertainty in the expected upper limit includes the experimental uncertainties. For the simplified DM LO models considered, mediator masses up to 950 GeV are excluded for values of m_{DM} less than 1 GeV.

The results for vector and axial-vector mediators are compared to constraints from the observed cosmological relic density of DM as determined from measurements of the cosmic microwave background by the Planck satellite experiment [?]. The expected DM abundance is estimated, separately for each model, using the thermal freeze-out mechanism implemented in the MADDM [?] framework and compared to the observed cold DM density $\Omega_c h^2 = 0.12$ [?], where Ω_c is the DM relic abundance and h is the dimensionless Hubble constant.

To enable a direct comparison with results from direct and indirect detection experiments, the 95% CL limits on the mediator mass for the vector and axial-vector models are translated to 90% CL limits on the spin-independent and spin-dependent DM–nucleon scattering cross sections, σ_{SI} and σ_{SD} respectively, following the prescriptions given in Ref. [?] and [?]. The exclusion contours for the vector and axial-vector models shown in Figure 2-32 are translated into the $\sigma_{\text{SI}} - m_{\text{DM}}$ and $\sigma_{\text{SD}} - m_{\text{DM}}$ planes shown in Figure 2-33. When compared to recent results by the CDMSLite [?], LUX [?], PandaX-II [?], XENON1T [?], and CRESST-II [?] collaborations, the limits

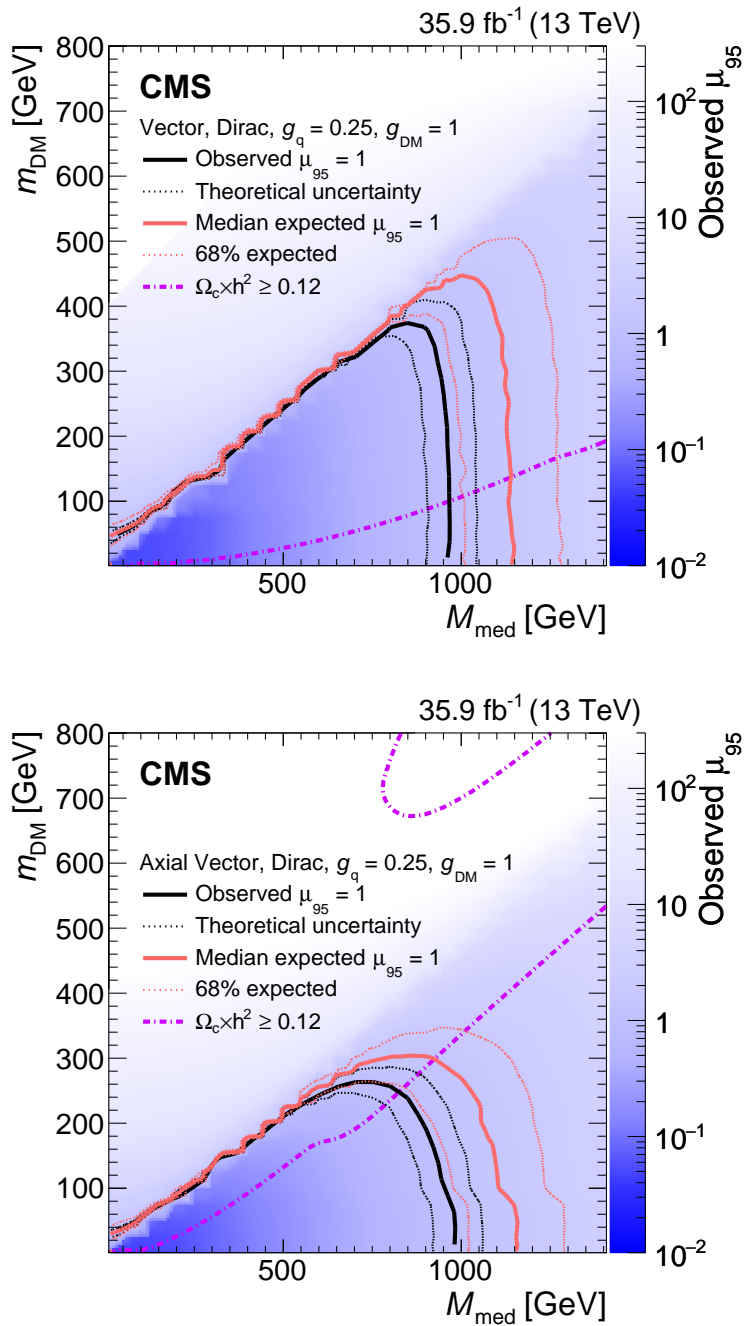


Figure 2-32: The ratio of 95% CL upper cross section limits to the theoretical cross section (μ_{95}), for DM simplified models with vector (top) and axial-vector (bottom) mediators, assuming $g_q = 0.25$ and $g_{\text{DM}} = 1$. Expected $\mu_{95} = 1$ contours are overlaid in red. The region under the observed contour is excluded. For DM simplified model parameters in the region below the lower violet dot-dash contour, and also above the corresponding upper contour in the right hand plot, cosmological DM abundance exceeds the density observed by the Planck satellite experiment.

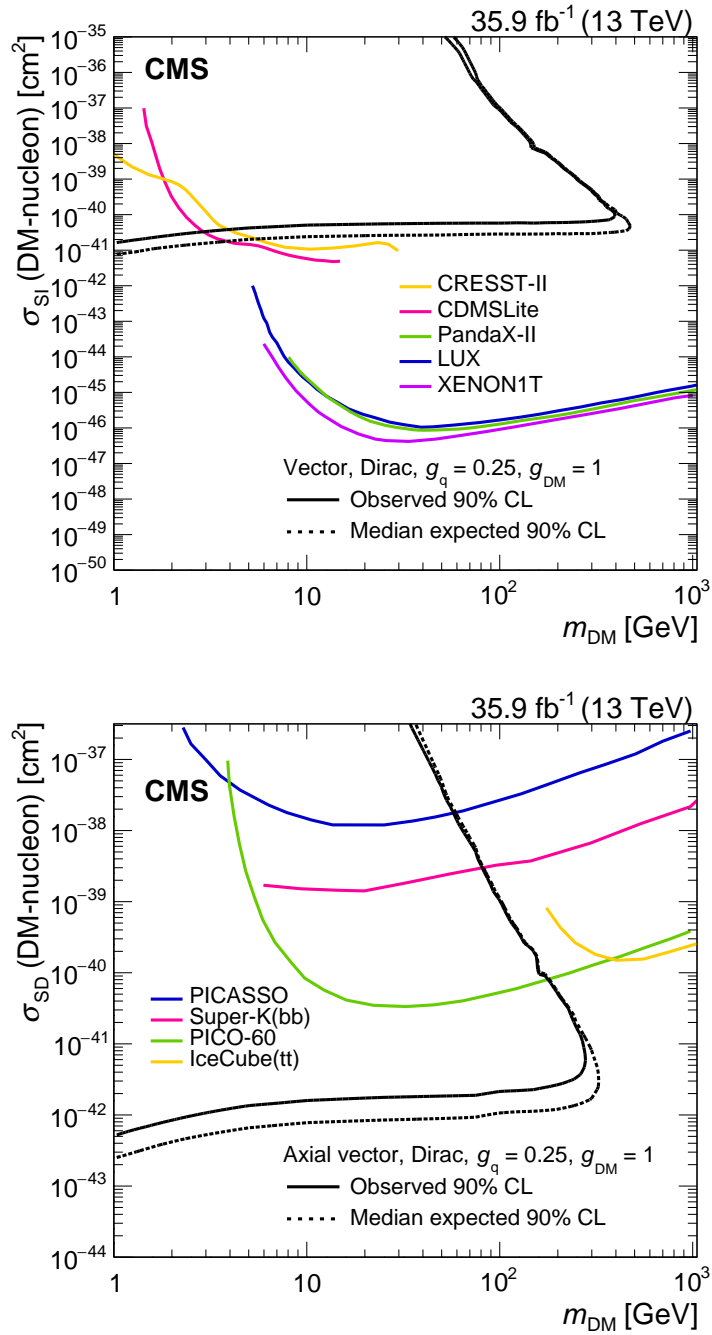


Figure 2-33: The 90% CL exclusion limits on the χ -nucleon spin-independent scattering cross sections involving the vector operator (top) and the χ -nucleon spin-dependent scattering cross sections involving the axial-vector operator (bottom) as a function of the m_{DM} . Simplified model DM parameters of $g_q = 0.25$ and $g_{\text{DM}} = 1$ are assumed. The region to the upper left of the contour is excluded. On the plots, the median expected 90% CL curve overlaps the observed 90% CL curve. Also shown are corresponding exclusion contours, where regions above the curves are excluded, from the recent results by the direct and indirect detection experiments listed in the text.

obtained from this search provide stronger constraints for DM masses less than 2 GeV for spin independent models. When compared to recent results by the PICO-60 [?], IceCube [?], PICASSO [?] and Super-Kamiokande [?] collaborations, the limits obtained from this search provide stronger constraints for DM masses less than 200 GeV for spin dependent models.